


Article

Palaeoenvironmental Evolution Based on Elemental Geochemistry of the Wufeng-Longmaxi Shales in Western Hubei, Middle Yangtze, China

Lulu Xu ¹, Saipeng Huang ^{2,3,*} , Mengdi Sun ², Yaru Wen ¹, Wei Chen ¹, Yanling Zhang ¹, Fan Luo ¹ and Hao Zhang ⁴

¹ Department of Shale Gas Geological Survey, Hubei Geological Survey, Wuhan 430000, China

² Key Laboratory of Continental Shale Hydrocarbon Accumulation and Efficient Development, Ministry of Education, Northeast Petroleum University, Daqing 163318, China

³ Departament de Mineralogia, Petrologia i Geologia Aplicada, Facultat de Ciències de la Terra, Universitat de Barcelona (UB), c/Martí i Franquès s/n, 08028 Barcelona, Spain

⁴ Hubei Coal Geological Exploration Institute, Wuhan 430000, China

* Correspondence: huangspcugb@hotmail.com

Abstract: The organic-rich shales found in the Wufeng–Longmaxi Formation are typically deposited in oxygen-deficient reducing environments. One of the primary sources of debate revolves around the question of whether the anoxic bottom water found in these shales is either euxinic or ferruginous, and this matter remains unresolved. Previous studies have mostly focused on the Wufeng–Longmaxi Formation as a whole in order to understand the key factors that control organic matter accumulation (OMA). However, research on OMA for each member, including the Wufeng Formation (WF), the lower Longmaxi Formation (LLM), and the upper Longmaxi Formation (ULM), has been insufficient. This paper aims to investigate the palaeoenvironmental conditions and OMA mechanisms of the Wufeng–Longmaxi shales in western Hubei by integrating data on total organic carbon (TOC) content, mineral compositions, major and trace elements, and iron speciation. The results indicate that the Wufeng–Longmaxi shales were deposited under highly restricted hydrographic conditions, except for relatively open and upwelling conditions in the upper WF. Silica in the upper WF was primarily biogenic origin and not hydrothermal. Ferruginous conditions were the primary redox conditions for organic-rich shales except for minor formations in the lower LLM that were deposited under euxinic conditions. Due to the tectonic uplift caused by the Kwangsi Orogeny in the upper LLM, the palaeoenvironment was characterized by a warmer and wetter climate, high terrigenous influx, oxic conditions, and low productivity as the result of the insufficient nutrients caused by the weak upwelling, leading to the turnover of graptolite biozones from LM5 to LM6. The factors influencing OMA changed vertically. TOC contents have a highly positive correlation with Al content, indicating that terrigenous influx was the main factor affecting OMA in the WF, which significantly differed from patterns found in other regions. This suggests that the sedimentation rate of organic matter was higher than the terrigenous dilution rate during the WF stage. The combination of redox conditions and productivity were the main factors affecting OMA in the LLM, while terrigenous influx was the key factor controlling OMA in the ULM, resulting in the dilution of organic matter. Regions in the eastern Yiling block, which are close to the Qinling Ocean, show better prospects for shale gas exploration. This research will further facilitate the development of shale gas in this area.

Keywords: palaeoredox conditions; palaeoproductivity; organic matter accumulation; Wufeng–Longmaxi shales; Western Hubei



Citation: Xu, L.; Huang, S.; Sun, M.; Wen, Y.; Chen, W.; Zhang, Y.; Luo, F.; Zhang, H. Palaeoenvironmental Evolution Based on Elemental Geochemistry of the Wufeng-Longmaxi Shales in Western Hubei, Middle Yangtze, China. *Minerals* **2023**, *13*, 502. <https://doi.org/10.3390/min13040502>

Academic Editor: Leszek Marynowski

Received: 7 February 2023

Revised: 23 March 2023

Accepted: 27 March 2023

Published: 31 March 2023



Copyright: © 2023 by the authors. Licensee MDPI, Basel, Switzerland. This article is an open access article distributed under the terms and conditions of the Creative Commons Attribution (CC BY) license (<https://creativecommons.org/licenses/by/4.0/>).

1. Introduction

During the late Ordovician to early Silurian period, black shales in the Wufeng–Longmaxi Formation were widespread on the upper and middle Yangtze Platforms [1–5], and are now

considered among the most promising hydrocarbon source rocks in South China [6,7]. In recent years, large-scale commercial developments in shale gas have achieved success in the Jiaoshiba block of the southeastern Sichuan Basin [8–10], and significant shale gas sources have been discovered in the Yiling block of western Hubei [2,3,11]. Consequently, considerable attention has been given to studying the palaeoenvironmental characteristics and organic matter accumulation (OMA) mechanisms of these blocks [5,12–15], which are vital for hydrocarbon generation and play a crucial role in determining the physical properties of shale reservoirs [1–3].

Previous studies have demonstrated that the Wufeng Formation (WF) and lower Longmaxi Formation (LLM) are organic-rich shales [3,13,16] deposited in the deep shelf [15,17] during a large-scale transgression [16,18]. These formations experienced warm and humid climates [5,14], dysoxic to anoxic conditions [13], and high productivity [3,15,16]. Moving upward to the upper Longmaxi Formation (ULM), the palaeoenvironmental became characterized by a warmer and wetter climate, high terrigenous influx [15,16], and the oxic conditions of bottom water due to the fall in sea level caused by the intense tectonic uplift of the Chuanzhong and Xuefeng uplifts [16,19], leading to the formation of organic-lean shales. Remarkably, the fall in sea level during the ULM stage was caused by the Kwanghsian Orogeny, which was a tectonic event dominated by horizontal movement with local vertical uplift movement, occurring from the southeast of Guangxi province to the northwest of Hunan province during the late Ordovician to the late Silurian [16,20,21], leading to the change of the environment from anoxic to oxic conditions, and turnover of the graptolite biozone LM5 in the Rhuddanian to LM6 in the Aeronian (Figure 1d) [21]. However, further research is necessary to fully understand the transition from LM5 to LM6.

Recently, iron speciation has been utilized to distinguish ferruginous and euxinic bottom water conditions in the Wufeng–Longmaxi Formation of the Sichuan Basin [22–25]. For instance, formations in the upper WF and lower LLM in well PY1 in the Sichuan Basin and in well Shenci-1 near the Qinling Ocean are apparently deposited under euxinic conditions [23]. However, the anoxic bottom water conditions in the Yichang area of western Hubei may be different from those in the regions near the depocenter of the Sichuan Basin and Qinling Sea in northern Yangtze, due to the different sedimentary facies. Therefore, further studies are required to determine the anoxic-ferruginous or anoxic-euxinic conditions of organic-rich shales in the WF and LLM in western Hubei. Additionally, the upwelling intensity of the bottom water may differ in different regions of the middle and upper Yangtze, owing to the varying sedimentary facies [12].

Generally, the OMA mechanism can be explained by the preservation model and productivity model [2,26], which indicate that redox conditions [5,27] and productivity [3,28] are the two main factors that influence OMA in the Wufeng–Longmaxi Formation. Previous studies have mostly focused on the Wufeng–Longmaxi Formation as a whole in order to understand the key factors that control organic matter accumulation (OMA). However, research on OMA for each member, including the WF, LLM, and ULM, has been insufficient.

Considering the inadequate research on the palaeoenvironmental evolution and OMA mechanism, we collected 24 samples from well YD1 of the Yiling block for geochemical testing to analyze the associated palaeoenvironmental conditions and OMA mechanism (Figure 1d). Moreover, we conducted further studies on the differences in geological conditions between the Yiling block and Jiaoshiba block [6,13]. The geological significance of this study lies in providing a geochemical basis for shale gas exploration in the area.

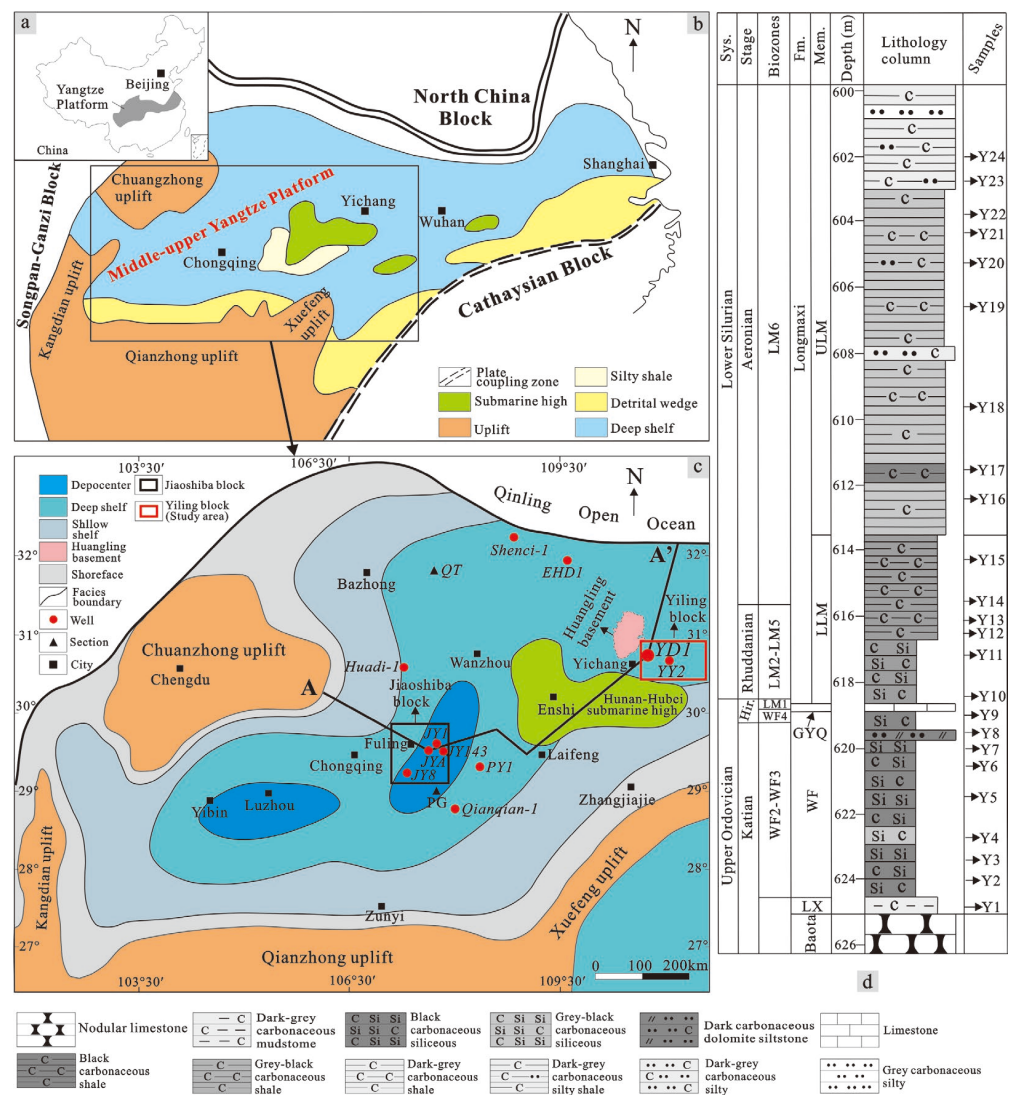


Figure 1. (a) Location of the Yangtze Platform in South China. (b) Palaeogeography of the Yangtze Platform in South China in the early Silurian (simplified from Zhang et al., 2019a [15]). (c) Palaeogeography of the middle-upper Yangtze Platform in the early Silurian showing the study area of the Yiling block in the southeastern Huangling basement (modified from Huang et al., 2020 [16]). (d) Lithostratigraphic column of well YD1 in the Yiling block showing the dark black siliceous rock in the WF, black siliceous rock and argillaceous shales in the LLM are organic-rich shales. Note: LX, WF, GYQ, LLM, and ULM are the abbreviations for the Linxiang, Wufeng, Guanyinqiao, and lower and upper Longmaxi formations, respectively.

2. Geological Setting

The Yangtze Platform, located in central China, is divided into the upper, middle, and lower regions based on sedimentary facies (Figure 1a). The middle-upper Yangtze Platform lies in the central and western parts of the region and is bordered by various uplifts and blocks, such as the Kangdian uplift to the southwest, Chuangzhong uplift to the northwest, Qinling Ocean and North China Block to the north, Qianzhong uplift to the south, and Xuefeng uplift and Cathaysia Block to the southeast (Figure 1b) [4,16]. During the late Ordovician to early Silurian, the Cathaysia Block subducted and extruded the middle-upper Yangtze Platform due to the Caledonian movement, forming a tectonic pattern with alternating uplifts and depressions and a semi-closed marine environment [4,15]. The Wufeng–Longmaxi shales were deposited in these depressions, with two main depocenters in the southern and eastern Sichuan Basin, respectively [29]. Additionally, the Hunan–Hubei submarine high

was formed between the cities of Chongqing and Yichang (Figure 1b and c) during the WF stage of the late Ordovician due to the collision between the Cathaysia Block and the Yangtze Platform [15,16,30].

The Fuling Jiaoshiba block, located in the southeastern Sichuan Basin and depicted in the black rectangle in Figure 1c, is the oldest commercial shale gas development block in China [6]. Recently, significant shale gas sources have also been discovered in the Yiling block in the study area [2], which is situated southeast of the Huangling basement and indicated by the red rectangle in Figure 1c. Well YD1, which targets the Wufeng–Longmaxi shales, is located in the Yiling block (Figure 1c). Generally, the Wufeng–Longmaxi Formation can be vertically divided into the Katian, Hirnantian, Rhuddanian, and Aeronian stages according to graptolite biozones [21]. According to lithological characteristics, it can be further divided into the LX, WF, GYQ, LLM, and ULM sections [2]. Among these, the LX section is composed of dark grey carbonaceous mudstone, the WF section is primarily composed of black carbonaceous siliceous rock interbedded with minor dolomite siltstone, the lower and upper LLM sections are mainly composed of black carbonaceous siliceous rock and black carbonaceous argillaceous shale, respectively, and the ULM section is mainly composed of dark grey carbonaceous shale (Figure 1d).

3. Methodology

3.1. Samples and Methods

Twenty-four fresh shale samples were collected from well YD1 in the Yiling block, comprising one sample from the LX (Y1), eight samples from the WF (Y2–Y9), six samples from the LLM (YA10–YA15), and nine samples from the ULM (YA16–YA24). After recovery, the samples were immediately placed in paper bags and analyzed by the State Key Laboratory of Biogeology and Environmental Geology in China for their TOC content, mineral compositions, major, trace, and rare earth elements, as well as iron speciation.

Among these, the TOC content was tested with a Multi EA 4000 carbon-sulfur tester, and 200 mesh samples of 0.1–0.3 g were treated with dilute hydrochloric acid to remove inorganic carbon and dried at 60–80 °C before the experiment, using the test methods and procedures following Chinese National Standard GB/T19145-2003. Mineral compositions were tested by a Rigaku SmartLab SE X-ray diffractometer, and approximately 5 g of evenly mixed sample powder was taken out for X-ray diffraction analysis, using test methods and procedures following China Petroleum Industry Standard SY/T 5163-2018. Major elements were analysed by a ZSXPrimus II X-ray fluorescence spectrometer, using test methods and procedures following Chinese National Standard GB/T 14506.28-2010. Trace and rare earth elements were determined with a multireceiver cup inductively coupled plasma source mass spectrometer, using test methods and procedures following Chinese National Standard GB/T14506.30-2010. Total iron content (FeT) was determined by the sulfosalicylic acid spectrophotometric method. Highly reactive iron (FeHR) includes iron in pyrite (Fepy), carbonate (Fecarb), magnetite (Femag), and ferric oxides (Feox). Fepy content was calculated from the concentration of pyrite sulfur (FeS₂) extracted using CrCl₂ reduction and precipitated as Ag₂S in silver nitrate traps [26]. Fecarb, Feox, and Femag fractions were extracted by the sequential procedure described in Poulton and Canfield (2005) [31] and measured by atomic absorption spectroscopy. All of the tests were conducted under an ambient laboratory temperature approximately 24 °C; relative humidity was maintained at 65%; and analytical errors were less than 5%.

3.2. Data Presentation

The enrichment factor (EF) can be applied to evaluate the degree of elements enrichment in sediments using the following equation [32]:

$$EF = (X/Al)_{\text{sample}} / (X/Al)_{\text{PAAS}} \quad (1)$$

where $(X/Al)_{\text{sample}}$ is the ratio of element X to Al measured in the sample, and $(X/Al)_{\text{PAAS}}$ is the ratio of element X to Al in post Archean Australian shale (PAAS) [33]. Generally,

$EF > 3$, $1 < EF < 3$, and $EF < 1$ were interpreted to reflect apparent enrichment, moderate enrichment, and depletion, respectively, relative to the PAAS standard [34].

In palaeomarine environments, the element concentration in sediments includes both non-biogenic and biogenic components. The concentration of elements derived from biogenic sources equals the total concentration in every sample minus its non-biogenic influx, and can therefore be calculated as follows [33,35]:

$$X_{\text{bio}} = X_{\text{Sample}} - Al_{\text{Sample}} \times (X/Al)_{\text{PAAS}} \quad (2)$$

where X_{bio} is the biogenic part of element X , and X_{sample} , and Al_{sample} are the contents of elements X and Al measured in the sample, respectively. $(X/Al)_{\text{PAAS}}$ is the ratio of X to Al in the PAAS.

The chemical index of alteration (CIA), which was originally proposed by Nesbitt and Young (1982) to determine the chemical weathering intensity of the provenance of clastic rock, was calculated following the formula below [36]:

$$\text{CIA} = \text{molar } (Al_2O_3 / [(Al_2O_3 + CaO^* + Na_2O + K_2O)] \times 100) \quad (3)$$

All major element concentrations are calculated in mole fractions. CaO^* refers to CaO in silicate. The method of indirect calculation of the value of CaO^* as follows [5]: $CaO_{\text{Remain}} = \text{molar } (CaO - P_2O_5 \times 10/3)$, if $\text{molar } (CaO_{\text{Remain}}) < \text{molar } (Na_2O)$, then $\text{molar } (CaO^*) = \text{molar } (CaO_{\text{Remain}})$; if $\text{molar } (CaO_{\text{Remain}}) > \text{molar } (Na_2O)$, then $\text{molar } (CaO^*) = \text{molar } (Na_2O)$. Generally, CIA values change greatly in different palaeoclimates, and CIA values range from 50 to 70, 70 to 80, and 80 to 100, indicating low, moderate, and high degrees of chemical weathering, respectively [14]. In general, weak weathering is associated with cold and arid climates, whereas intense weathering is associated with hot and wet climates. New K was introduced by K metasomatism during diagenesis, resulting in low CIA values. Therefore, it was necessary to correct it. Generally, the CIA values before K metasomatism (CIA_{corr}) value can be calculated by Al_2O_3 – CaO^* + Na_2O – K_2O ternary diagrams [35].

Additionally, La–Th–Sc and Th–Sc–Zr/10 ternary discrimination diagrams are used to infer the tectonic settings [37,38]. The CIA_{corr} value, Sr/Cu, and Rb/Sr ratios are used to reconstruct palaeoclimate conditions [39,40]. The $Al/(Al + Fe + Mn)$ and $(Fe+Mn)/Ti$ ratios are used to evaluate hydrothermal deposition [15,41]. The $Si_{\text{bio}}/(Si_{\text{bio}} + Fe_{\text{bio}} + Al + Ca_{\text{bio}})$ ratio is used to distinguish biogenic sources, where a ratio of > 0.8 indicates an absolute biogenic source [17,35]. The Al content is used to study the level of terrigenous influx [15,16]. The V/Cr, Ni/Co, U/Th, and Fe/Al ratios are used to reflect palaeoredox conditions [14,42–45]. A $Fe_{\text{py}}/Fe_{\text{HR}}$ vs. $Fe_{\text{HR}}/Fe_{\text{T}}$ discrimination diagram is used to distinguish euxinic and ferruginous conditions [46,47]. The Mo vs. TOC discrimination diagram and proxy $Co \times Mn$ are used to evaluate palaeohydrography [48,49]. The proxies Si_{bio} , $(Ni + Cu + Zn)_{\text{bio}}$, P/Ti, and Cu/Al are used to evaluate palaeoproductivity [3,13,15,40]. The La_N/Yb_N ratio is used to reflect the deposition rate [35], where subscripts N represents the chondrite normalization [50].

4. Results

4.1. Lithology and Graptolite Biozones

Core and thin section images are shown in Figure 2. The LX is composed of dark grey carbonaceous mudstone (Figure 2a). The WF is primarily composed of black carbonaceous siliceous rock (Figure 2b) with larger quartz grains and many bioclasts (Figure 2c) interbedded with minor dolomite siltstone (Figure 2d) containing much calcite and dolomite (Figure 2e). *Rectograptus* of the WF2-3 graptolite biozones was clearly observed in the bedding plane (Figure 2f). The LLM is mainly composed of black carbonaceous argillaceous shale with clear laminated bedding (Figure 2g), the mineral compositions are slightly oriented, and the particle size of quartz is obviously smaller than that in the WF (Figure 2h). *Campograptus* of graptolite biozone LM6 was clearly observed in the bedding plane (Figure 2i). The ULM is mainly composed of dark grey carbonaceous shale (Figure 2j), and the mineral compositions

are apparently oriented with many hydromica minerals (Figure 2k). Demirastrite graptolites of the LM6 biozone are clearly observed in the bedding plane (Figure 2l).

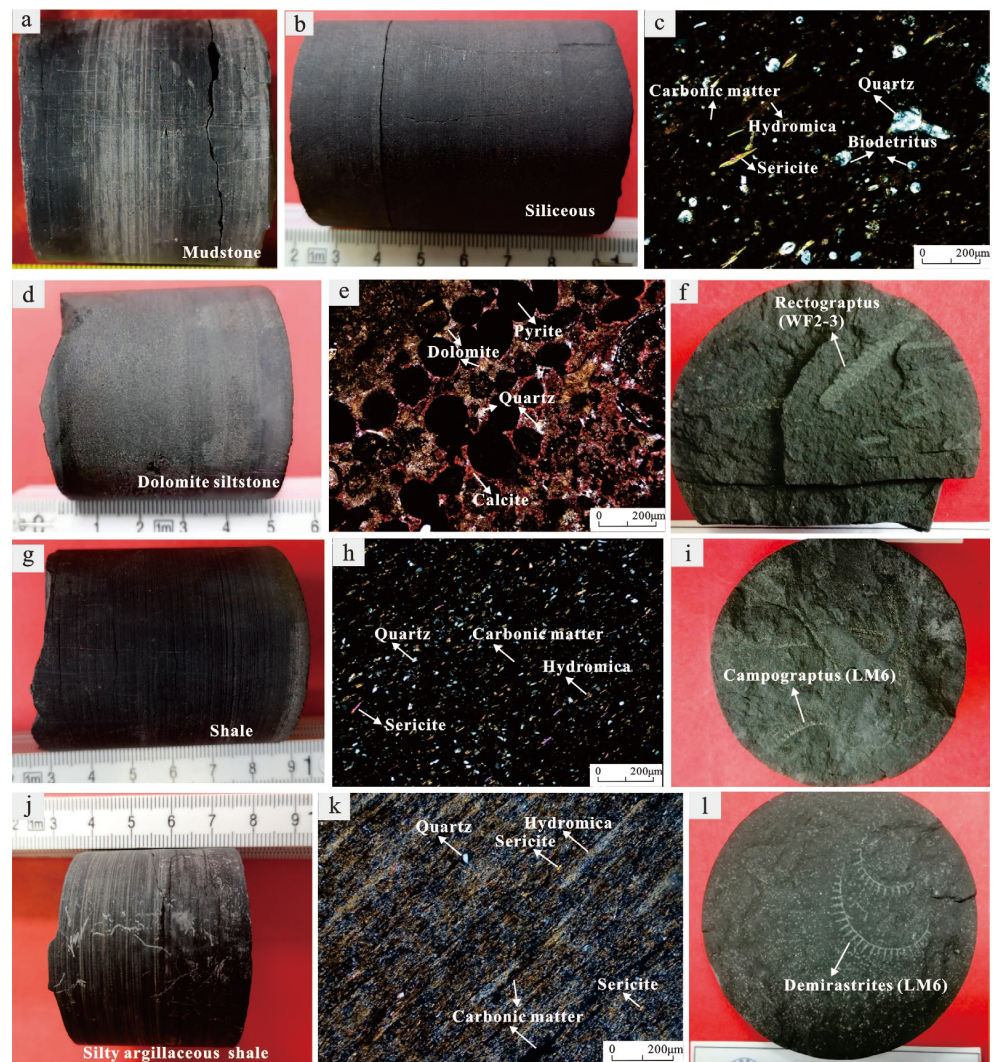


Figure 2. (a) Core image of dark grey carbonaceous mudstone in the LX, sample Y1 with a depth of 625 m. (b,c) Core and thin section images of black carbonaceous siliceous rock in the WF, sample Y9 with a depth of 618.46 m. (d,e) Core and thin section images of grey-black carbonaceous dolomite siltstone in the WF, sample Y8 with a depth of 619.5 m. (f) Rectograptus image of graptolite biozones WF2-3 in the WF, depth 621.26 m. (g,h) Core and thin section images of black carbonaceous shale in the LLM, sample Y13 with a depth of 616.1 m. (i) Campograptus image of graptolite biozone LM6 in the LLM, depth 615.6 m. (j,k) Core and thin section images of dark grey carbonaceous silty shale in the UMX, sample Y20 with a depth of 605.26 m. (l) Demirastrite image of graptolite biozone LM6 in the ULM, depth 610.71 m.

4.2. TOC Content

Generally, organic-rich and organic-lean shales are characterized by TOC contents of greater than 2%, and lower than 2%, respectively [51]. The TOC values are presented in Table 1 and Figure 3a. The TOC content is less than 1% in the LX with a value of only 0.7%, and it ranges from 1.90% to 4.94% (avg. 3.21%), 2.61% to 6.29% (avg. 4.14%), and 0.76% to 2.74% (avg. 1.50%) in the WF, LLM, and ULM, respectively. The results show that the WF and LLM include organic-rich shales, and the LX and ULM include organic-lean shales. Additionally, the results show a significant decrease in TOC content from 6.18% of sample Y13 to 3.05% of sample Y14 in the LLM.

Table 1. TOC and major elements contents of the Wufeng–Longmaxi Formation in well YD1.

Sample No.	TOC (%)	SiO ₂ (%)	TiO ₂ (%)	Al ₂ O ₃ (%)	Fe ₂ O ₃ (%)	MnO (%)	MgO (%)	CaO (%)	Na ₂ O (%)	K ₂ O (%)	P ₂ O ₅ (%)	Fe _T (%)	Fe _{py} (%)	Fe _{HR} (%)	Al (%)	Si _{bio} (%)	Si _{bio} /(Si _{bio} + Fe _{bio} + Al + Ca _{bio})	Al/(Al + Fe + Mn)	(Fe + Mn)/Ti	ClAcorr	P/Ti	Fe _{py} /Fe _{HR}	Fe _{HR} /Fe _T	Fe _T /Al	
Y24	0.76	61.5	0.69	16.79	6.55	0.06	2.68	0.48	1.21	3.9	0.11	4.59	0.79	1.44	8.89	2.66		0.24	0.66	11.19	76.8	0.12	0.55	0.31	0.52
Y23	0.80	61.6	0.7	17.1	6.38	0.05	2.71	0.43	1.18	4.05	0.11	4.47	0.68	1.2	9.05	2.23		0.21	0.67	10.73	77.4	0.11	0.57	0.27	0.49
Y22	1.74	60.2	0.67	16.41	6.34	0.05	2.59	0.51	1.04	3.92	0.11	4.44	0.97	1.57	8.69	2.64		0.66	11.14	78.7	0.12	0.62	0.35	0.51	
Y21	1.37	60.4	0.67	16.62	6.65	0.05	2.66	0.55	1.04	3.95	0.11	4.65	1.02	1.67	8.80	2.42		0.22	11.68	79.0	0.12	0.61	0.36	0.53	
Y20	1.11	59.3	0.7	16.88	6.44	0.05	2.71	0.62	1.09	4.04	0.1	4.51	0.89	1.62	8.94	1.48		0.15	10.83	78.2	0.10	0.55	0.36	0.50	
Y19	1.73	61	0.69	16.12	6.23	0.05	2.6	0.61	1.04	3.84	0.1	4.36	0.94	1.61	8.53	3.48		0.30	10.63	78.3	0.11	0.58	0.37	0.51	
Y18	1.58	61.3	0.65	15.74	6.23	0.04	2.5	0.42	0.98	3.76	0.11	4.36	1.06	1.6	8.33	4.20		0.65	11.26	79.0	0.12	0.66	0.37	0.52	
Y17	2.74	59.3	0.62	14.24	6.33	0.03	2.28	0.57	1.1	3.32	0.13	4.43	0.85	2.45	7.54	5.57		0.41	11.97	75.9	0.15	0.35	0.55	0.59	
Y16	1.71	62.8	0.6	14.8	6.2	0.04	2.38	0.36	1.01	3.51	0.1	4.34	1.06	2.14	7.84	6.34		0.64	12.14	77.7	0.12	0.50	0.49	0.55	
Y15	2.61	61.1	0.6	13.8	6.61	0.04	2.36	0.94	0.98	3.3	0.1	4.63	1.67	2.71	7.31	7.11		0.46	12.94	77.0	0.12	0.62	0.59	0.63	
Y14	3.05	58.4	0.62	13.83	6.57	0.03	2.08	0.75	1.09	3.27	0.12	4.6	1.23	3.27	7.32	5.80		0.42	12.43	75.4	0.14	0.38	0.71	0.63	
Y13	6.18	70.4	0.48	8.9	3.65	0.02	1.24	0.96	0.98	1.98	0.11	2.56	1.41	2.09	4.71	19.04		0.79	8.93	69.7	0.17	0.67	0.82	0.54	
Y12	6.29	48.9	0.6	11.01	7.55	0.06	2.41	2.5	1.27	2.33	0.2	5.29	3.19	4.41	5.83	5.76		0.38	14.81	68.8	0.24	0.72	0.83	0.91	
Y11	3.45	82	0.26	4.99	1.87	0.02	0.6	1.28	0.61	0.99	0.07	1.31	0.83	1.22	2.64	30.55		0.90	8.49	67.8	0.20	0.68	0.93	0.50	
Y10	3.23	82	0.26	4.55	1.98	0.03	0.71	1.75	0.66	0.88	0.07	1.38	0.78	1.28	2.41	31.19		0.90	9.03	64.2	0.20	0.61	0.92	0.58	
Y9	2.99	78	0.24	6.64	2.7	0.02	0.62	1.45	0.61	1.47	0.06	1.89	1.31	1.93	3.52	26.09		0.86	13.23	73.0	0.18	0.68	1.02	0.54	
Y8	2.58	34.7	0.37	8.34	4.34	0.22	3.62	18.9	0.58	1.85	0.03	3.04	1.9	3.18	4.42	3.28		0.15	14.45	77.4	0.06	0.60	1.05	0.69	
Y7	2.05	82.1	0.2	3.73	1.85	0.04	0.62	2.87	0.46	0.75	0.06	1.29	0.82	1.25	1.97	32.55		0.89	11.05	67.6	0.22	0.66	0.97	0.66	
Y6	3.86	83.9	0.22	4.57	1.66	0.01	0.63	0.7	0.42	1.04	0.05	1.16	0.66	0.98	2.42	32.07		0.92	8.86	72.9	0.17	0.67	0.84	0.48	
Y5	4.49	74.3	0.44	8.07	2.91	0.02	1.28	0.94	0.65	1.99	0.08	2.03	0.85	1.34	4.27	22.17		0.83	7.77	75.2	0.13	0.63	0.66	0.48	
Y4	1.9	89.9	0.13	2.95	0.94	0.01	0.41	0.81	0.26	0.66	0.04	0.66	0.27	0.46	1.56	37.39		0.95	8.54	73.7	0.22	0.59	0.70	0.42	
Y3	2.88	77.2	0.33	7.12	2.81	0.03	1.03	1.41	0.47	1.78	0.07	1.96	0.78	1.25	3.77	24.99		0.85	10.05	77.9	0.15	0.62	0.64	0.52	
Y2	4.94	63.6	0.68	13.98	4.29	0.03	2.17	0.65	0.92	3.71	0.11	3	0.55	1.01	7.40	7.99		0.55	7.42	78.1	0.12	0.54	0.34	0.41	
Y1	0.7	60.8	0.84	17.07	5.52	0.03	2.81	0.95	1.01	4.6	0.09	3.86	0.56	1.12	9.04	1.89		0.19	7.71	79.5	0.08	0.50	0.29	0.43	
PAAS	/	62.8	1	18.9	7.22	0.11	2.2	1.3	1.2	3.7	0.16	/	/	/	/	/		/	/	/	/	/	/	/	

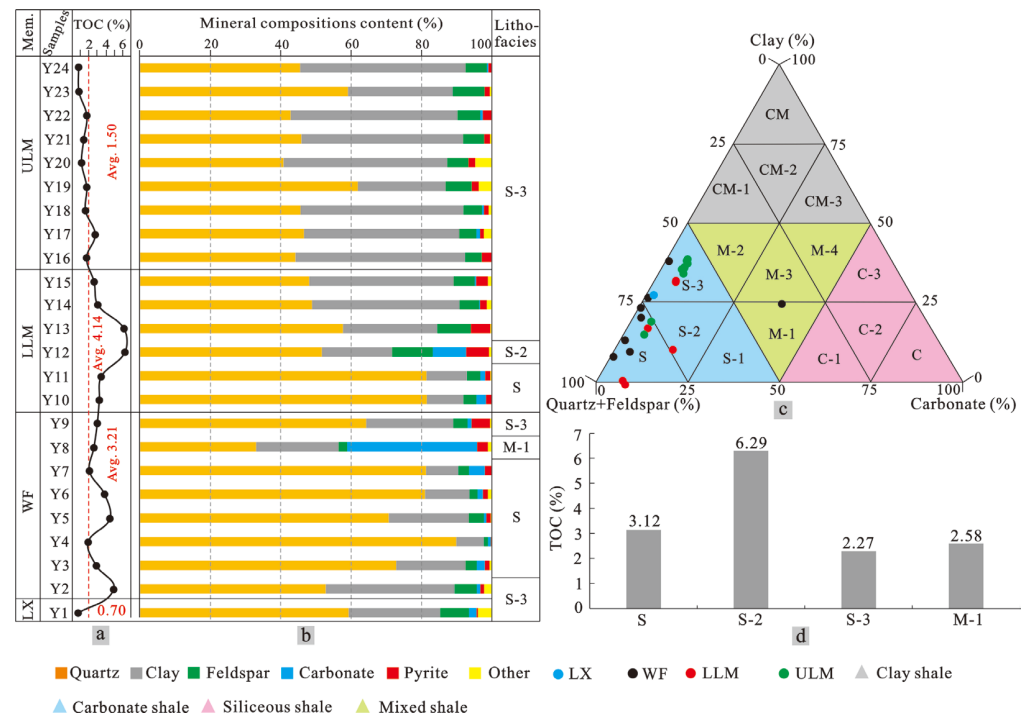


Figure 3. (a) Vertical variation in TOC content shows that the WF and LLM include organic-rich shales. (b) The percentage of bulk mineral compositions shows that quartz contents decrease and clay contents increase from the bottom to the top. (c) The lithofacies classification shows that most samples are plotted in the field of siliceous shales. (d) TOC contents in different subclass lithofacies show that S-2 and S have higher TOC values. Note: CM, CM-1, CM-2, and CM-3 represent mudstone, siliceous argillaceous shale, argillaceous shale, and calcareous argillaceous shale, respectively. C, C-1, C-2, and C-3 represent limestone, siliceous calcareous shale, calcareous shale, and argillaceous calcareous shale, respectively. S, S-1, S-2, and S-3 represent siliceous rock, calcareous siliceous shale, siliceous shale, and argillaceous siliceous shale, respectively. M-1, M-2, M-3, and M-4 represent calcareous siliceous mixed shale, argillaceous siliceous mixed shale, mixed shale, and argillaceous calcareous mixed shale, respectively.

4.3. Mineral Compositions and Lithofacies

Mineral compositions are mainly composed of quartz and clay in all of the samples, for which quartz contents reach 59.3%, 33.0%–89.9% (avg. 68.3%), 48.1%–81.5% (avg. 61.6%), and 40.8%–61.9% (avg. 48.0%) in the LX, WF, LLM, and ULM, respectively, showing a decreasing trend from the bottom to the top. In contrast, clay contents reach 26.0%, 7.8%–36.6% (avg. 19.6%), 10.4%–41.9% (avg. 25.3%), 24.9%–48.2% (avg. 42.2%), showing an increasing trend from bottom to top. Contents of feldspar, carbonate, and pyrite are low in all of the samples, and the feldspar, carbonate, and pyrite contents are higher in the ULM, WF, and LLM, respectively (Figure 3b).

Shale can be divided into four lithofacies types (siliceous, calcareous, clay, and mixed shales) [52]. These can further be subdivided into sixteen lithofacies types according to a three-end element map of clay, carbonate, and felsic rocks content [53]. The results show that most samples are plotted in the siliceous shale field except for sample Y8 of the WF, which is plotted in the mixed shale field, for which organic-rich shales in the WF and LLM are primarily plotted as subclass lithofacies type S, and organic-lean shales in the LX and ULM are primarily plotted as subclass lithofacies type S-3 (Figure 3c).

4.4. Major and Trace Elements

The results regarding major elements are listed in Table 1. Major oxides mainly include SiO_2 and Al_2O_3 in all of the formations, where organic-rich shales have higher contents of SiO_2

in the WF (34.74%–89.92%, avg. 72.97%) and LLM (48.92%–82.04%, avg. 67.13%), and organic-lean shales have higher contents of Al_2O_3 in the LX (17.07%) and ULM (14.24%–17.10%, avg. 16.08%). Additionally, organic-rich shales are relatively rich in CaO, while organic-lean shales are relatively rich in MgO, Na_2O , and K_2O . The EF value shows that Si, Ca, Na, P, and Fe contents in the organic-rich shales are higher than those of the organic-lean shales with moderate to apparent enrichment relative to PAAS (Figure 4a).

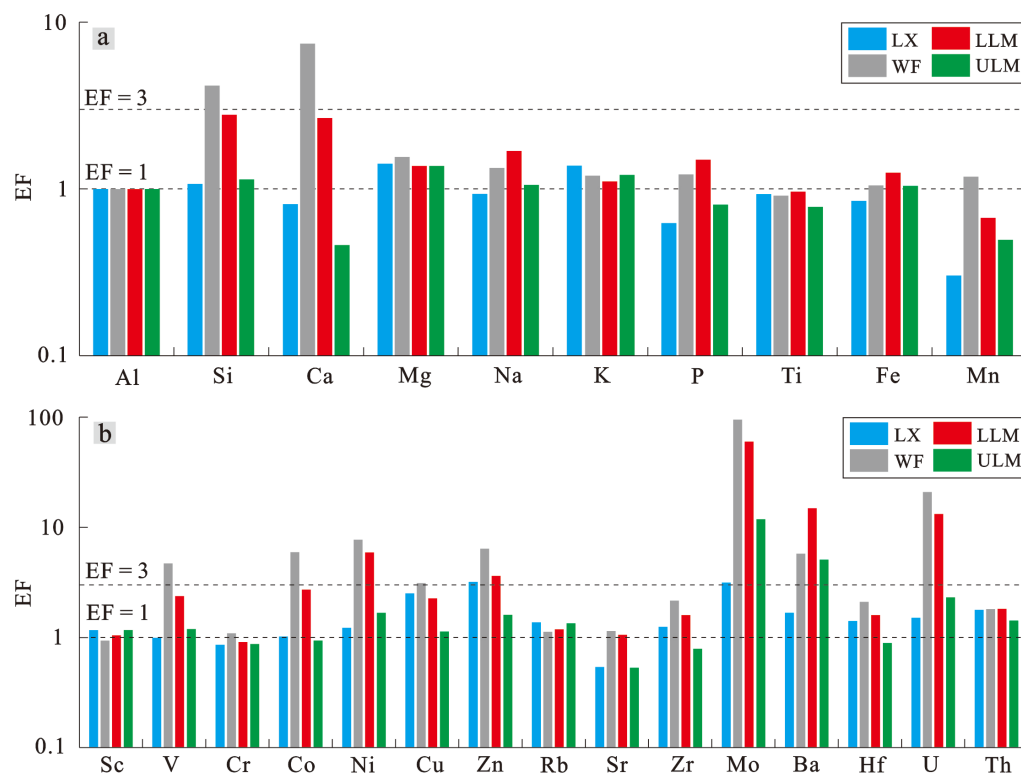


Figure 4. (a) Enrichment factors of the major element's values show that Si, Ca, Na, P, and Fe contents in organic-rich shales are higher than those of organic-lean shales, with moderate to apparent enrichment contents compared to those of PAAS. (b) Enrichment factors of the trace elements show that V, Co, Ni, Cu, Zn, Mo, Ba, and U contents in organic-rich shales are higher than those of organic-lean shales, with moderate to apparent enrichment relative to those of PAAS. The dotted line with EF = 1 highlights enrichment or depletion, and the dotted line with EF = 3 highlights apparent or moderate enrichment.

The results of the trace elements are listed in Table 2. V, Co, Ni, Mo, and U are rich in organic-rich shales, while Sc, Cr, Rb, Hf, and Th are rich in organic-lean shales. The EF values show that V, Co, Ni, Cu, Zn, Mo, Ba, and U contents in organic-rich shales are higher than those of organic-lean shales with moderate to apparent enrichment relative to PAAS (Figure 4b).

Table 2. Trace elements contents of the Wufeng–Longmaxi Formation in well YD1.

Sample No.	Y24	Y23	Y22	Y21	Y20	Y19	Y18	Y17	Y16	Y15	Y14	Y13	Y12	Y11	Y10	Y9	Y8	Y7	Y6	Y5	Y4	Y3	Y2	Y1	PAAS	
Sc (ppm)	16.33	16.85	16.52	16.87	17.54	15.45	15.16	14.15	13.90	13.75	13.40	7.65	10.20	3.88	3.52	4.82	1.57	2.69	3.96	8.00	2.44	6.31	16.02	16.84	16	
V (ppm)	139.18	134.34	158.23	175.24	166.84	171.58	166.72	131.83	125.06	134.55	144.00	218.36	228.99	128.61	99.23	123.32	77.90	83.90	279.34	571.00	234.40	96.02	329.21	134.65	150	
Cr (ppm)	83.48	86.69	84.90	87.13	87.04	81.64	77.71	74.68	71.64	70.79	71.10	47.48	59.30	28.37	23.18	26.20	4.11	19.80	34.60	64.70	27.00	56.40	115.48	85.18	110	
Co (ppm)	18.08	18.26	18.68	20.02	19.15	18.37	18.31	16.00	17.66	18.66	24.40	16.34	29.40	26.89	30.98	16.02	18.20	70.00	22.51	21.60	66.77	24.77	12.00	21.14	23	
Ni (ppm)	64.23	64.53	87.47	92.86	83.46	87.25	83.68	64.84	75.25	110.77	144.00	132.13	340.22	93.91	97.50	120.29	195.00	154.00	105.60	150.00	105.29	98.04	83.62	60.83	55	
Cu (ppm)	50.48	39.34	46.07	51.68	48.93	48.63	50.48	49.17	47.11	64.75	75.30	58.07	78.58	31.12	26.74	32.53	14.80	19.30	51.26	82.40	32.03	74.03	159.46	113.71	50	
Zn (ppm)	124.79	111.17	123.66	122.29	124.99	120.96	107.02	107.72	102.87	116.80	119.00	140.06	355.78	85.89	69.91	110.44	308.00	102.00	135.52	258.00	135.07	172.61	244.17	245.27	85	
Rb (ppm)	184.08	194.66	193.04	193.38	193.17	180.57	175.65	164.80	167.13	162.99	153.00	88.32	117.18	42.99	37.66	53.26	54.80	29.40	46.27	87.80	29.80	71.74	172.53	197.96	160	
Sr (ppm)	86.66	89.16	107.48	88.65	90.98	86.69	96.85	91.79	74.15	84.31	85.90	65.02	260.65	60.25	53.33	58.84	257.00	61.90	38.54	59.70	33.19	53.26	81.58	97.36	200	
Zr (ppm)	146.84	144.92	150.92	146.13	144.68	139.68	137.26	137.50	125.47	130.30	144.00	134.52	213.58	91.31	152.60	146.99	186.00	243.00	56.26	113.00	77.54	98.31	216.38	236.25	210	
Mo (ppm)	2.16	3.25	8.17	5.45	6.20	10.52	6.27	31.29	12.75	16.23	34.10	45.00	53.05	13.54	12.68	11.75	33.00	33.50	43.26	85.20	7.51	6.58	25.20	2.84	1	
Ba (ppm)	1606.3	2037.3	6096.1	1374.8	1202.8	1662.1	5645.0	4164.0	1127.6	879.7	958.0	873.2	26770.3	896.7	1025.6	1284.2	2732.0	1106.0	893.3	951.0	743.9	995.6	818.6	981.3	650	
Hf (ppm)	3.88	3.98	4.03	3.97	3.88	3.63	3.60	3.72	3.34	3.58	3.89	3.61	5.53	2.21	2.89	3.18	7.98	5.15	1.32	2.95	0.87	2.69	4.31	6.37	5	
U (ppm)	4.82	4.91	6.78	4.98	6.13	5.90	5.83	8.43	6.38	10.13	14.50	14.97	51.17	8.54	14.53	25.56	87.70	21.50	8.06	13.50	4.31	12.88	7.89	4.22	3.1	
Th (ppm)	17.54	17.61	18.57	18.54	18.63	17.69	16.78	17.29	16.12	17.21	17.50	12.65	17.71	6.69	7.05	10.96	11.50	6.15	5.81	11.10	3.24	9.94	18.80	23.42	14.6	
La (ppm)	45.95	47.08	48.20	48.57	47.14	45.75	45.31	44.07	42.62	43.59	44.10	32.83	46.47	18.88	23.05	29.09	62.10	25.50	19.57	34.10	11.10	26.54	52.84	60.33	38	
Yb (ppm)	2.79	2.93	2.91	2.95	2.80	2.78	2.62	2.73	2.51	2.69	2.84	2.27	3.90	1.46	1.67	2.27	1.36	2.10	1.21	2.19	1.03	1.57	4.43	3.89	2.8	
Sr/Cu	1.72	2.27	2.33	1.72	1.86	1.78	1.92	1.87	1.57	1.30	1.14	1.12	3.32	1.94	1.99	1.81	17.36	3.21	0.75	1.04	0.72	1.04	0.72	0.51	0.86	/
Rb/Sr	2.12	2.18	1.80	2.18	2.12	2.08	1.81	1.80	2.25	1.93	1.78	1.36	0.45	0.71	0.91	0.21	0.47	1.20	1.47	1.20	0.90	1.35	2.11	2.03	/	
Sr/Ba	0.05	0.04	0.02	0.06	0.08	0.05	0.02	0.02	0.07	0.10	0.09	0.07	0.01	0.07	0.05	0.05	0.09	0.06	0.04	0.06	0.04	0.05	0.10	0.10	/	
V/Cr	1.67	1.55	1.86	2.01	1.92	2.10	2.15	1.77	1.75	1.90	2.03	4.60	3.86	4.53	4.28	4.71	18.95	4.24	8.07	8.83	8.68	1.70	2.85	1.58	/	
U/Th	0.28	0.28	0.37	0.27	0.33	0.33	0.35	0.49	0.40	0.59	0.83	1.18	2.89	1.28	2.06	2.33	7.63	3.50	1.22	1.39	1.22	1.33	1.30	0.42	0.18	/
Ni/Co	3.55	3.53	4.68	4.64	4.36	4.75	4.57	4.05	4.26	5.94	5.90	8.08	11.57	3.49	3.15	7.51	10.71	2.20	4.69	6.94	1.58	3.96	6.97	2.88	/	
Cu/Al	5.68	4.35	5.30	5.87	5.47	5.70	6.06	6.52	6.01	8.86	10.28	12.32	13.48	11.78	11.10	9.25	3.35	9.77	21.19	19.29	20.51	19.64	21.55	12.58	/	
Mo/TQC ($\times 10^{-4}$)	2.85	4.04	4.70	3.98	5.59	6.08	3.97	11.42	7.46	6.22	11.18	7.28	8.43	3.92	3.93	3.93	12.79	16.34	11.21	18.98	3.95	2.28	5.10	4.06	/	
Co \times Mn ($\times 10^{-8}$)	0.84	0.71	0.72	0.78	0.74	0.71	0.57	0.37	0.55	0.58	0.57	0.25	1.37	0.42	0.72	0.25	3.10	2.17	0.17	0.33	0.52	0.58	0.28	0.49	/	
(Ni + Cu + Zn) _{bio} (ppm)	70.72	49.03	92.23	99.75	87.68	94.79	82.95	78.58	76.46	153.60	199.27	240.79	663.90	160.75	148.41	196.50	441.22	237.80	246.44	409.27	242.73	273.10	346.71	248.21	/	
La _N /Yb _N	10.96	10.71	11.06	10.96	11.22	10.98	11.54	10.77	11.32	10.78	10.35	9.62	7.94	8.61	9.18	8.55	30.44	8.10	10.76	10.38	7.20	11.27	7.95	10.34	9.05	

4.5. Iron Speciation

The iron speciation results are listed in Table 1. Fe_{py} and Fe_{HR} contents are characterized as follows: the LLM (avg. 1.52% and 2.50%, respectively) > the ULM (avg. 0.92% and 1.70%, respectively) > the WF (avg. 0.89% and 1.43%, respectively) > the LX (0.56% and 1.12%, respectively). Average contents of Fe_T are characterized as follows: the ULM (avg. 4.46%) > the LX (3.86%) > the LMX (avg. 3.29%) > the WF (avg. 1.88%).

5. Discussion

5.1. Tectonic Setting

Trace element discrimination diagrams have also been used to distinguish tectonic settings [37,38]. In the diagrams of La-Th-Sc and Th-Sc-Zr/10 (Figure 5a,b) proposed by Bhatia and Crook (1986) [37], most samples mainly plot within or near the field of the active continental margin, and minor samples fall within the field of the continental island arc, which is consistent with that of the Huadi-1 well in the southeastern Sichuan Basin [38]. These results show that from the late Ordovician to the early Silurian, the subduction of the Proto-Tethys oceanic crust towards the South China Plate led to the convergence and compression between the Cathaysia Block and Yangtze Platform [16], forming a tectonic setting of mainly active continental margins.

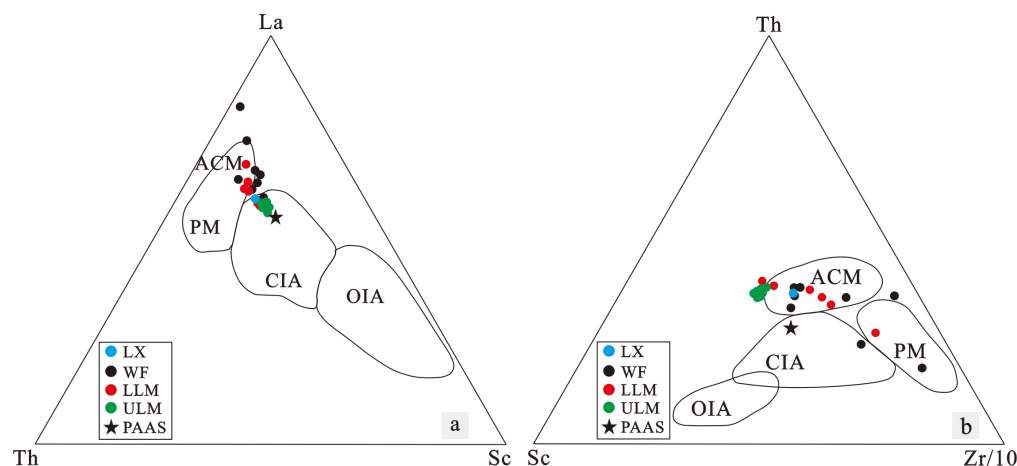


Figure 5. (a) La–Th–Sc and (b) Th–Sc–Zr/10 ternary diagrams (modified from Ge et al., 2019 [38]) showing mainly active continental margin tectonic settings. Note: OIA, CIA, ACM, and PM are the abbreviations for the oceanic island arc, continental island arc, active continental margin, and passive margin, respectively.

5.2. Palaeoenvironment

5.2.1. Palaeoclimate

The palaeoclimate controls levels of the humidity and weathering, thus affecting terrigenous influx and the sediment supply in sedimentary rocks [41]. The chemical index of alteration (CIA) has been widely used to reconstruct the palaeoclimate, and the formula of CIA is shown in Section 3.2 [5,16,35]. The Sr/Cu ratio is an effective indicator for evaluating palaeoclimate change, with ratios of <5, 5–10, and >10 indicating humid, semihumid-semiarid, and arid palaeoclimates, respectively [40,54]. Additionally, because Rb is relatively stable under weathering, whereas Sr is prone to leaching during weathering, the Rb/Sr ratio is often used to study palaeoclimate in provenance, with high and low ratios indicating a warm and humid climate with a high degree of weathering and an arid climate with a low degree of weathering, respectively [39,55].

The Al_2O_3 – CaO^* + Na_2O – K_2O ternary diagrams (Figure 6) show that the predicted weathering trend line (T') is parallel to the Al_2O_3 – CaO^* + Na_2O line and points towards the endmember of Al_2O_3 . Starting from the K_2O end member, crossing the sample data point and intersecting with T' , the CIA_{corr} values can be obtained [35].

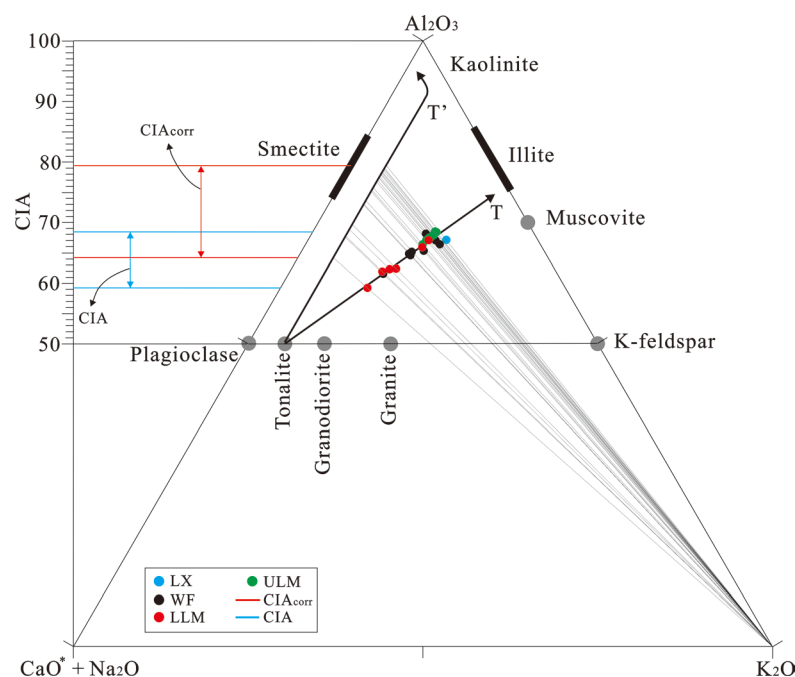


Figure 6. Al_2O_3 – $\text{CaO}^* + \text{Na}_2\text{O}$ – K_2O ternary diagrams exhibiting weathering degree (all in mole percentages). The CIA_{corr} values of most samples range from 70 to 80, indicating a moderate degree of chemical weathering and a warm and humid palaeoclimate. Note: T and T' are the actual and predicted weathering trends, respectively.

The results show that the CIA_{corr} value is highest in the LX with the value of 79.5, and it ranges from 67.6 to 78.1 (avg. 74.5), 64.2 to 77.0 (avg. 70.5), 75.9 to 79.0 (avg. 77.9), and 57.4 to 75.7 (avg. 72.1), respectively, which indicate mainly a moderate degree of chemical weathering and imply a warm and humid climate in the Wufeng–Longmaxi Formation. Comparatively speaking, the CIA_{corr} values of the LX and ULM are higher than that of the WF and LLM, which indicates a much warmer and wetter climate in the organic-lean shales (Table 1; Figures 6 and 7).

As shown in Figure 7, the Sr/Cu ratios of most samples are lower than 5 except for sample Y8 of dolomite siltstone from the WF, which has a Sr/Cu ratio of 17.4, denoting a primarily warm and humid climate in the Wufeng–Longmaxi Formation and a much drier climate in the formation enriched with carbonate minerals.

The profiles of Rb/Sr ratios and CIA_{corr} values are nearly consistent, which shows that from the bottom to the top, the climate was moderately warm and humid in the LX and the lower WF. Then, there was slight warmth and humidity in the upper WF. Further upwards, cold and arid conditions occurred in the GYQ due to Gondwanan continental glaciation at the end of the late Ordovician [16,56]. Subsequently, with the melting of Gondwanan continental glaciers in the early Silurian [16,18], the climate gradually changed to slight warmth and humidity in the lower LLM. Then, the Kwangsi Orogeny intensified in the Yangtze Platform with strong tectonic uplift, leading to the sea level dropping rapidly [20,21] and the palaeoenvironment changing significantly. Remarkably, there is a significant decrease in TOC content from 6.18% in sample Y13 below the red dotted line to 3.05% in sample Y14 above the red dotted line, a significant increase in Al content from 8.9% to 13.83%, and a significant increase in Rb/Sr ratios and CIA_{corr} value, indicating that the climate rapidly changed from slightly warm and humid in the lower LLM to moderately warm and humid in the upper LLM. Accordingly, the significant variation in the palaeoclimate during the LLM stage was one of the key factors that led to the turnover of graptolite biozones from LM5 to LM6. After this, the climate was much hotter and wetter in the ULM with high Rb/Sr ratios, leading to a high degree of chemical weathering [13,16].

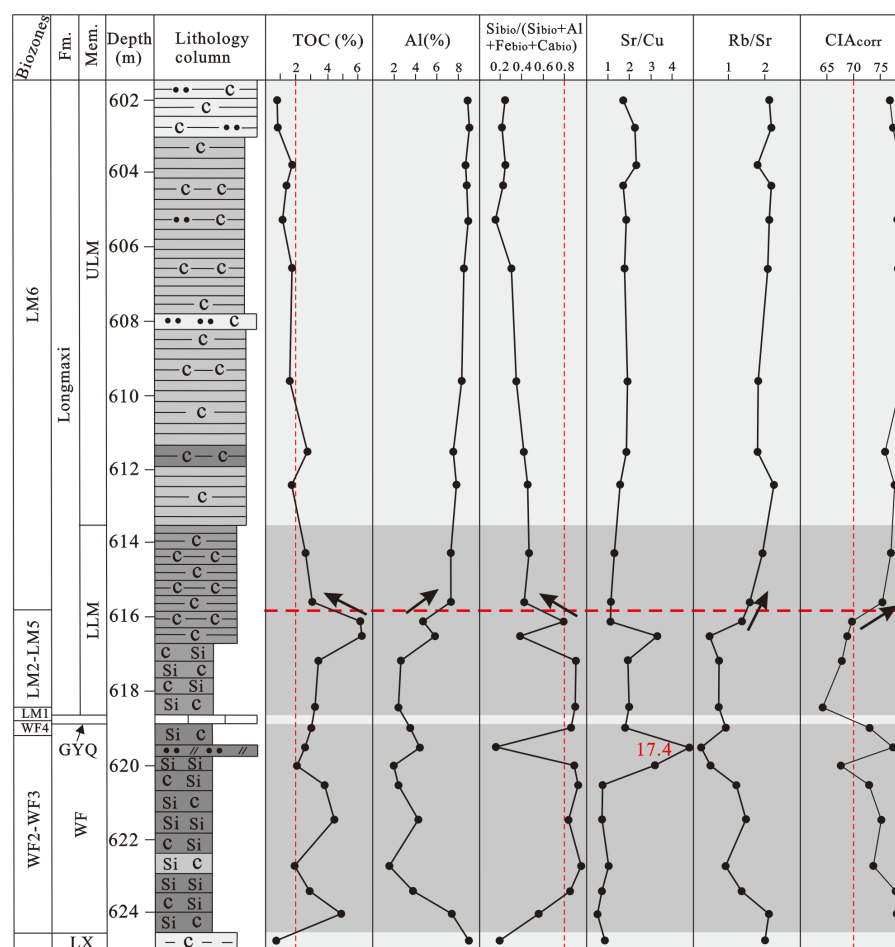


Figure 7. Vertical variation in TOC contents, terrigenous influx proxy Al contents, biogenic source discrimination proxy $Si_{bio}/(Si_{bio} + Fe_{bio} + Al + Ca_{bio})$, palaeoclimate proxies Sr/Cu and Rb/Sr, and CIA_{corr} of the Wufeng–Longmaxi Formation in well YD1, showing that the organic-rich shales in the WF and LLM mainly deposited in the warm and humid climate, and the organic-lean shales in the LX and ULM mainly deposited in a warmer and wetter climate. Remarkably, the significant variation of palaeoenvironment caused by the Kwanghsian Orogeny [20,21] directly led to the turnover of graptolite biozones from the LM5 in Rhuddanian to the LM6 in Aeronian. Note: The red dotted line represents the boundary of Rhuddanian and Aeronian.

The variation of the palaeoclimate in well YD1 is consistent with that of well YY2 in the Yiling block [2] and well JY8 in the Jiaoshiba block [16], indicating that the palaeoclimate of the middle Yangtze Platform is similar to that of the upper Yangtze Platform. Additionally, we found that the climate of organic-rich shales in the WF and LLM is neither cold and arid like that of the GYQ nor hot and wet like that of organic-lean shales in the LX and ULM. The climate during the WF and LLM stages can be described as moderately warm and humid.

5.2.2. Origin of Silica and Terrigenous Influx

Previous studies have identified three primary sources of siliceous sediments in marine environments: hydrothermal fluids, siliceous organisms, and silica-rich terrigenous clastics [57]. In sedimentary rocks, Fe and Mn are generally enriched with hydrothermal deposits, and in typical sediments influenced by hydrothermal events, the $(Fe + Mn)/Ti$ and $Al/(Al + Fe + Mn)$ ratios are generally valued at >15 and <0.4 , respectively [41]. The analysis shows that all of the samples plot in the nonhydrothermal field, implying that silica mainly had a nonhydrothermal origin (Figure 8a).

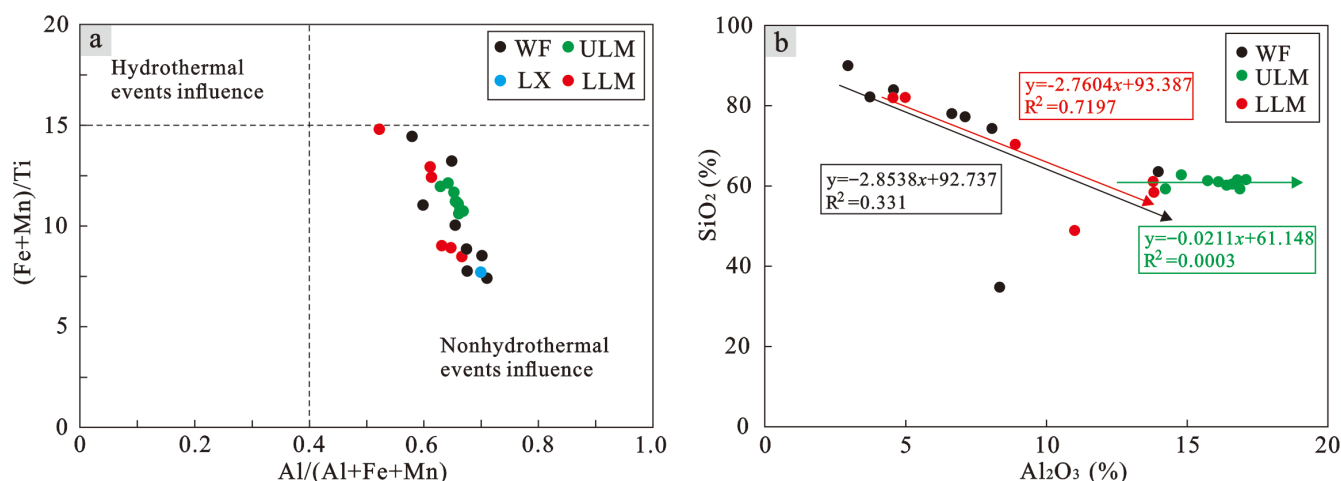


Figure 8. (a) Crossplots of (Fe + Mn)/Ti vs. Al/(Al + Fe + Mn) showing that the silica mainly had a nonhydrothermal origin. (b) Crossplots of SiO₂ vs. Al₂O₃ showing a negative correlation in the WF and LLM, implying a mainly source of biogenic silica and no significant correlation in the ULM, implying that silica probably had a mixed biogenic and terrigenous clastic origin.

Al is generally considered an indicator element for terrigenous clastic material [5,15]; therefore, the crossplots of SiO₂ vs. Al₂O₃ are usually used to distinguish terrestrial and biogenic silica with a positive correlation, no apparent correlation, and a negative correlation reflecting mainly terrestrial silica, mixed origin of terrestrial and biogenic silica, and biogenic silica, respectively [35]. The results show that silica mainly had a biogenic origin in the WF and LLM, and a mixed terrestrial and biogenic origin in the ULM (Figure 8b). The results show that graptolites are the main sources of biogenic silica in the Wufeng–Longmaxi Formation [13,48] (Figure 2), and there is also a small amount of sponge spicules and radiolarians [13,48,58].

Additionally, the Si_{bio}/(Si_{bio} + Fe_{bio} + Al + Ca_{bio}) ratios of most samples of organic-rich shales in the WF and the lower LLM are higher than 0.8, indicating an absolute biogenic silica [17,59]. In contrast, the low Si_{bio}/(Si_{bio} + Fe_{bio} + Al + Ca_{bio}) ratios of samples from the LX, upper LLM, and ULM suggest that silica partly originated from terrigenous clasts. Remarkably, the Si_{bio}/(Si_{bio} + Fe_{bio} + Al + Ca_{bio}) ratios of the LM6 graptolite biozone of the Aeronian above the red dotted line are significantly lower than those of the LM5 graptolite biozone of the Rhuddanian below the red dotted line (Table 1; Figure 7). The reason is that, as a result of the Kwangsian Orogeny [60], the sea level dropped rapidly due to the large-scale uplift in the Yangtze Platform, which led to a decrease in the quantity of graptolites and contents of biogenic silica.

The influx of terrigenous clastic material is a key factor that influences black shale composition and OMA [15,35,42]. The results show that Al contents are higher in organic-lean shales in the LX (9.04%) and ULM (avg. 8.51%) and lower in organic-rich shales in the WF (avg. 3.67%) and LLM (avg. 5.04%) (Table 1; Figure 7). The variation of Al content in the Yiling block is consistent with that in the JY8 well and PG section of the southeastern Sichuan Basin (Figure 1c) [16,34]. Specifically, Al content of the LM6 graptolite biozone in the Aeronian is significantly higher than those of the LM5 graptolite biozone in the Rhuddanian (Table 1; Figure 7), which indicates that as a result of the Kwangsian Orogeny [58], the Chuangzhong and Qianzhong uplifts were significantly uplifted, coupled with a warm and wet climate (Figure 7) [16], resulting in a significant increase in terrigenous influx.

As shown in Figure 9, Al contents show a highly positive correlation with the palaeoclimate proxy Rb/Sr ratio, implying that terrigenous influx is significantly influenced by the palaeoclimate. Generally, warm and humid palaeoclimates lead to a relatively high degree of weathering [14,35,36], which facilitates the weathering and transport of terrigenous clasts from surrounding palaeohighs into the Yangtze Sea. Additionally, Xuefeng uplift

was exposed to erosion and became one of the source areas during the early Silurian [16], which is a direct influencing factor leading to a much stronger terrigenous influx in the ULM (Table 1 and Figure 7).

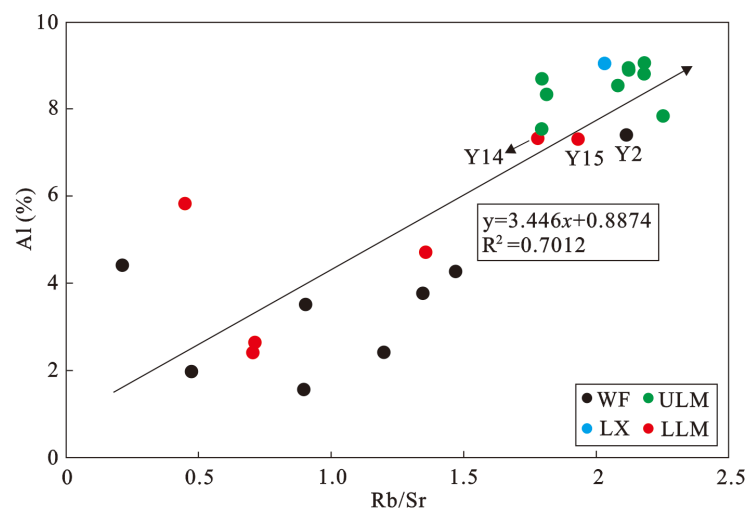


Figure 9. Crossplots of terrigenous influx proxy Al vs. palaeoclimate proxy Rb/Sr show that higher terrigenous influx is closely associated with the warmer and wetter palaeoclimate in the LX, lower WF (sample Y2), upper LLM (samples Y14 and Y15), and ULM.

5.2.3. Palaeoredox Conditions

Some trace elements such as Ni, Co, V, Cr, Th, U, and Mo in sedimentary rocks are redox sensitive. Thus, they are usually used to reflect redox conditions due to their differentiation under different bottom water conditions [32]. The ratios of some trace elements such as V/Cr, Ni/Co, and U/Th are widely used tools in the reconstruction of benthic oceanic redox conditions since these trace metals can coprecipitate with organic matter or metal sulphides under anoxic conditions [61,62].

In general, $V/Cr < 2$, $Ni/Co < 5$, and $U/Th < 0.75$ indicate oxic conditions; $2 < V/Cr < 4.25$, $5 < Ni/Co < 7$, and $0.75 < U/Th < 1.25$ indicate dysoxic conditions; and $V/Cr > 4.25$, $Ni/Co > 7$, and $U/Th > 1.25$ indicate anoxic conditions [14,15,44,45,61,62]. Additionally, iron speciation proxies Fe_{HR}/Fe_T and Fe_{py}/Fe_{HR} are usually used to evaluate the bottom water redox conditions of ancient oceans [46,63]. In general, Fe_{HR}/Fe_T values < 0.38 and > 0.38 indicate oxic and anoxic conditions, respectively. For anoxic conditions, $Fe_{py}/Fe_{HR} < 0.7$ – 0.8 and > 0.7 – 0.8 indicate ferruginous and euxinic conditions, respectively [47]. Furthermore, the Fe_T/Al ratio is an effective indicator with which to evaluate bottom water redox conditions [43]. Generally, Fe_T/Al ratios are valued at > 0.5 in deep-water basins under anoxic conditions. Remarkably, the Fe_T/Al ratios in the sediments under euxinic conditions are 2–3 times those of the sediments under oxic conditions.

The results show that the curve graphs of V/Cr and U/Th are relatively consistent, and they are apparently different from the Ni/Co curve graph (Figure 10). Therefore, the V/Cr and U/Th ratios are used to evaluate redox conditions. From the bottom to the top, the LX and the bottom of the WF are mainly deposited under oxic conditions that rapidly changed to anoxic conditions in the middle-upper WF. At the end of the late Ordovician, the GYQ was largely deposited under oxic conditions in the middle Yangtze Platform as a result of the significant drop in global sea level [56]. Subsequently, with the melting of the Gondwanan continental glaciers and the influx of the freshwater in the early Silurian, the sea level rose rapidly, and the seawater formed a stable stratified water body due to density differences, which resulted in clear vertical difference between the surface and bottom layers with the low content of dissolved oxygen in the bottom water [18,64,65], leading to mainly anoxic conditions of bottom water in the lower LLM. During the upper LLM and ULM stages, as the Kwangsi Orogeny with compressive stress continuously

transferred from the South China Plate to the Yangtze Platform in the northwest, Xuefeng uplift was elevated rapidly and even exposed to erosion [16,60], leading to the fall of sea level in the long term. Thus, from sample Y14 in the upper LLM, the bottom water started to change from anoxic to mainly oxic, which is not beneficial to the preservation of organic matter such as the species of graptolite, radiolarian, and sponge spicule, leading to a significant drop in TOC content above the red dotted line.

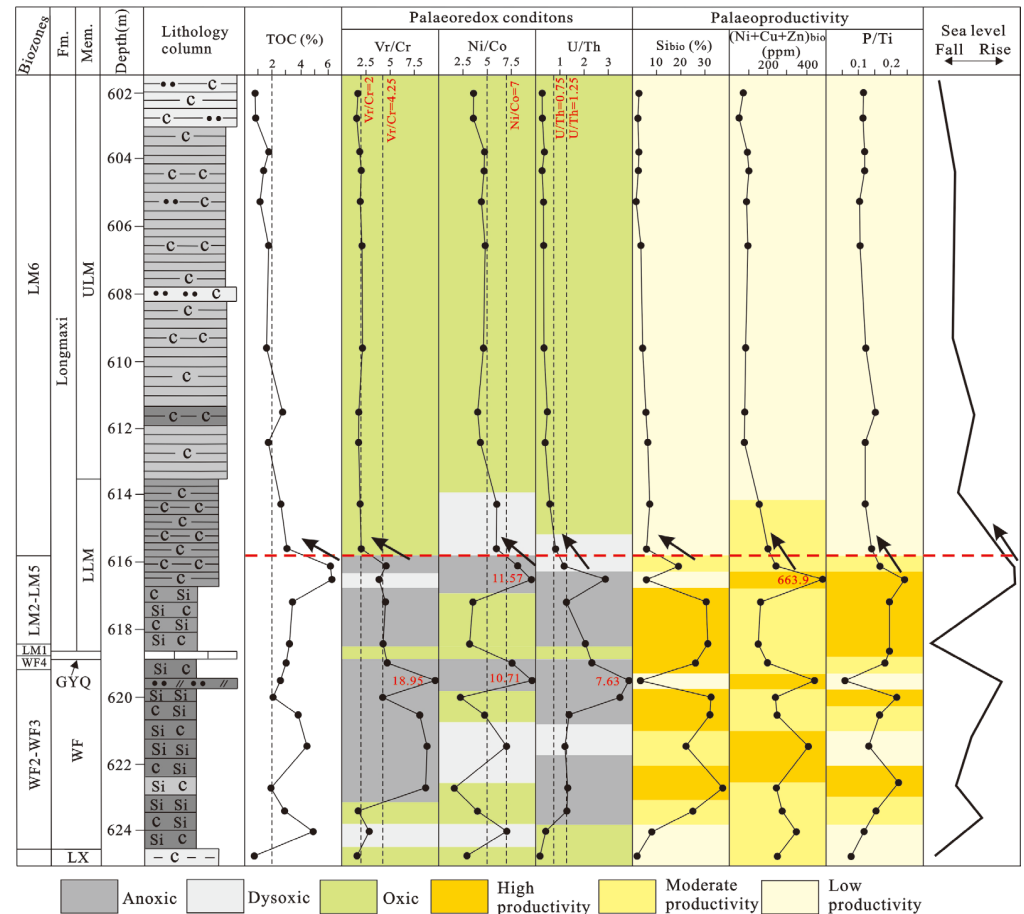


Figure 10. Vertical variations in TOC content; palaeoredox proxies V/Cr, Ni/Co, and U/Th and palaeoproductivity proxies Si_{bio} , $(Ni + Cu + Zn)_{bio}$, and P/Ti of the Wufeng–Longmaxi Formation in well YD1 showing mainly anoxic conditions and high productivity in organic-rich shales of the middle-upper WF and the lower LLM.

As shown in Figure 11, the average Fe_{py}/Fe_{HR} and Fe_T/Al ratios of the LX, WF, LLM, and ULM are 0.50 and 0.43, 0.62 and 0.52, 0.61 and 0.63, and 0.55 and 0.53, respectively. Therefore, the bottom water in the LLM shows the highest level of anoxia, especially in sample Y12, and the bottom water is in a euxinic condition with peak values of Fe_{py}/Fe_{HR} ratios, Fe_T/Al ratios, and TOC content. Subsequently, the Fe_{py}/Fe_{HR} ratios significantly decreased from graptolite biozones LM5 to LM6, which implies that bottom water conditions transformed from ferruginous conditions in the Rhuddanian to oxidic conditions in the Aeronian (Figure 11a).

The Fe_{py}/Fe_{HR} vs. Fe_{HR}/Fe_T discrimination diagram shows that the LX and ULM were mainly deposited under oxidic conditions and that the WF and the LLM were primarily deposited under ferruginous conditions except for sample Y12 with a Fe_{py}/Fe_{HR} ratio of 0.72, implying euxinic conditions during this period (Figure 11b). There are three main reasons for the euxinic conditions found in sample Y12 from the LLM. with the first reason regards the melting of Gondwanan continent glaciers and the influencing of the salinity stratification, which led to an anoxic reducing environment in bottom water [18,65]. In

addition, in the early Silurian, tectonic compression and uplift continuously transferred from Xuefeng uplift in the southeast to the Yangtze Platform in the northwest [16], leading to strong tectonic subsidence and the formation of a deep-water basin during the Longmaxi stage. Furthermore, the seawater in the study area was confined by the Huangling basement (a submarine high), Hunan–Hubei submarine high, and Xuefeng uplift (Figure 1c), leading to a strongly restricted basin, which was beneficial for forming euxinic conditions.

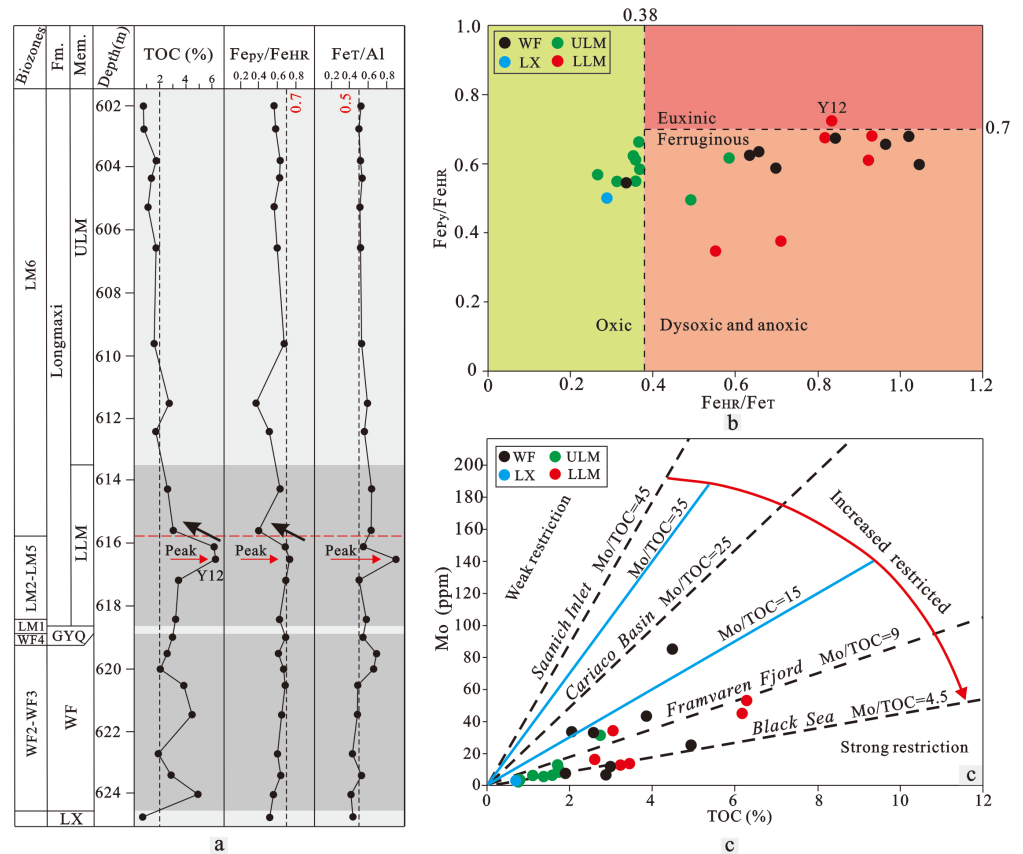


Figure 11. (a) Vertical variation in palaeoredox condition proxies Fe_{py}/Fe_{HR} and Fe_T/Al in the Wufeng–Longmaxi Formation in well YD1 showing mainly ferruginous conditions except for one sample in the lower LLM that was deposited under euxinic conditions. (b) Crossplots of redox proxies Fe_{py}/Fe_{HR} vs. Fe_{HR}/Fe_T showing that LX and ULM were mainly deposited under oxic conditions and WF and LLM were primarily deposited under ferruginous conditions. (c) Crossplots of TOC vs. Mo showing that the Mo/TOC values of most samples are lower than 15×10^{-4} [15], indicating a strong degree of restriction.

The results show that the redox conditions of organic-rich shales in well YD1 of the Yiling block are similar to those in well Qianqian-1 [24] and different from those in well PY1 in the southeastern Sichuan Basin [23] and well Shenci-1 in northern Hubei [22]. The bottom water of well Qianqian-1 is mainly under oxic to dysoxic conditions because it is close to the Qianzhong uplift, and the bottom water is primarily under ferruginous to euxinic conditions in well PY1 in the southeastern Sichuan Basin and well Shenci-1 in northern Hubei close to the Qingling Ocean because of the oxygen-deficient environment in the deep shelf resulting in anoxic conditions. In contrast, the bottom water of well YD1 mainly shows oxic to dysoxic conditions except for minor formations deposited under euxinic conditions (Figure 11a,b), which infer a much shallower palaeocean in the Yiling block relative to the regions of the southeastern Sichuan Basin and northwestern Qinling Ocean.

Overall, the redox conditions of the Wufeng–Longmaxi Formation in the Yiling block show oxic conditions mainly in the LX, lower WF, upper LLM, and ULM, and anoxic conditions in the middle-upper WF and lower LLM, which is consistent with the Jiaoshiba

block [13]. Previous studies have shown that anoxic conditions are directly caused by the rapid transgressive events during the middle-upper WF and lower LLM stages [12,16]. Oxidic conditions are mainly attributed to the shallow water environment present during the LX and lower WF stages [12], while oxidic conditions are directly caused by the fall of sea level as a result of the continuous elevation of the Chuanzhong and Xuefeng uplifts during the upper LLM and ULM stages [16].

5.2.4. Palaeohydrography

Hydrographic conditions are essential to controlling nutrients obtained from the deep ocean to the shallow shelf, and thus can influence palaeoproductivity and OMA [35]. Usually, Mo is a common redox-sensitive element and is abundant only under sulfurated conditions [66], and the Mo–TOC discrimination diagram is usually used to determine hydrographic conditions. Basins can be classified as presenting three levels of restriction: strongly restricted ($\text{Mo}/\text{TOC} < 15 \times 10^{-4}$), moderately restricted ($15 \times 10^{-4} < \text{Mo}/\text{TOC} < 35 \times 10^{-4}$), and weakly restricted ($\text{Mo}/\text{TOC} > 35 \times 10^{-4}$) [67]. The results show that the average Mo/TOC ratios in the LX, WF, LLM, and ULM are 4.06×10^{-4} , 9.32×10^{-4} , 6.83×10^{-4} , and 5.56×10^{-4} , respectively (Table 2), and the Mo/TOC ratios of most samples are lower than 15×10^{-4} except for two samples in the WF with Mo/TOC ratios of greater than 15×10^{-4} , indicating mainly a strongly restricted basin in the Wufeng–Longmaxi Formation, and minor formations in the middle-upper WF were deposited under a moderately restricted basin (Figure 11c).

Given that the Co \times Mn values were observed to show significant differences between sediments from the upwelling and restricted settings, Sweere et al. (2016) [49] proposed that Co \times Mn values can be used to evaluate upwelling intensity, with values of <0.4 and >0.4 indicating upwelling and restricted settings, respectively. The results show that most samples plot within the restricted field except for minor samples of organic-rich shales mainly found in the WF that fall within the open and upwelling field, implying that the WF showed much stronger upwelling intensity, followed by the lower LLM, and that the LX, upper LLM and ULM showed weak upwelling intensity (Figure 12a,b), leading to the insufficient nutrients transportation from the deep ocean to the shallow shelf [2,3], which was not beneficial for the survival of graptolites at the stages of the upper LLM and ULM. Thus, the graptolite abundance and quantity rapidly decreased due to the oligotrophic seawater caused by the weak upwelling, which was probably another important factor that led to the turnover of graptolite biozones from LM5 to LM6.

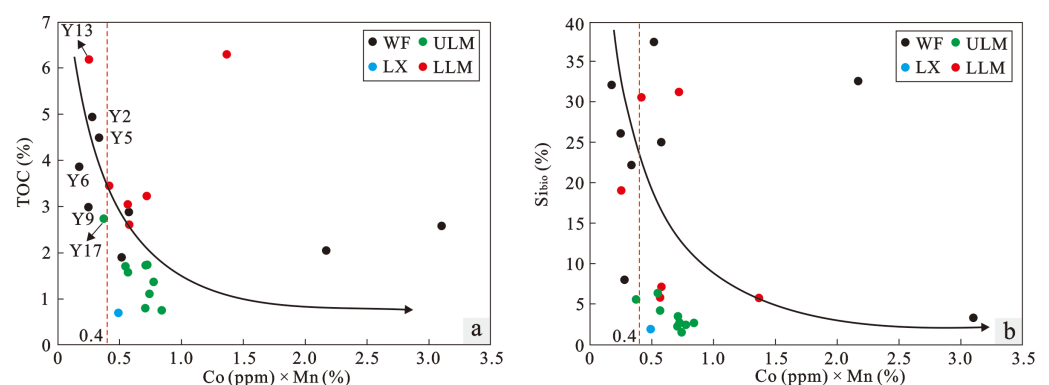


Figure 12. (a) Crossplots of TOC content vs. Co \times Mn values and (b) crossplots of Si_{bio} content vs. Co \times Mn values indicating that the WF showed much stronger upwelling and a negative correlation between palaeoproductivity and upwelling intensity, implying that strong upwelling could bring nutrients from the deep ocean to the shallow shelf, leading to high palaeoproductivity.

Overall, both the Mo/TOC and Co \times Mn proxies show that the Wufeng–Longmaxi Formation of well YD1 mainly formed in a highly restricted setting except for minor samples that formed in a moderately restricted setting in the WF. In fact, the hydrographic conditions of the Wufeng–Longmaxi Formation are closely related to the sedimentary

location [12]. The sedimentary basin in the Yiling block is a highly restricted setting, as it is surrounded by the Xuefeng uplift, the Hunan–Hubei submarine high, and Huangling basement, a submarine high formed in the Sinian (Figure 1c) [68]. The southeastern Sichuan Basin, where wells PY1 and JY143 are located, is a moderately restricted setting because it is a depocentre that has a relatively good connection with the Qinling Ocean [12,68]. The sedimentary basin, where well EHD1 is located, is weakly restricted because it is much closer to the Qinling Ocean, showing the highest level of upwelling intensity [12].

5.2.5. Palaeoproductivity

TOC is the surface productivity of the ocean reflected in sediments, and thus, it is regarded as a most direct primary productivity indicator [69]. Cu, Ni, and Zn are micronutrients for marine microbes that are complex with organic matter under reducing conditions [15,32]. Thus, these elements are typical indicators of marine primary productivity. A large number of radiolarians and graptolites in the shale confirmed the biological contribution of silica in the Wufeng–Longmaxi Formation. Thus, Si_{bio} can be used as a productivity indicator [16,70]. P is involved in most of the metabolic activities of organisms and is usually regarded as one of the most extensively applicable and reliable productivity indicators [71]. To eliminate the terrestrial part of P content, proxy P/Ti is used to estimate primary productivity [72].

The results show that the profiles of TOC, Si_{bio} , $(Ni + Cu + Zn)_{bio}$ and P/Ti generally have similar variation trends with only a small difference in local formation (Figure 10). In the LX and lower WF, palaeoproductivity was low to moderate, apparently increased to high palaeoproductivity in the middle-upper WF, and suddenly decreased in the upper WF. Palaeoproductivity was generally low in the GYQ, which was caused by mass extinction as a result of Hirnantian glaciation at the end of the late Ordovician [14,16]. In the lower LLM in the early Silurian, palaeoproductivity was high and peaked in sample Y12 of graptolite biozone LM5, and then gradually decreased in graptolite biozone LM6 in the upper LLM shown above the red dotted line, maintaining a low level of palaeoproductivity throughout the ULM stage. The decline in palaeoproductivity in the upper LLM and ULM is closely related to the Kwangsian Orogeny, which resulted in the uplift of the Longmaxi Formation and the fall of sea level [20,21,61], and the sedimentary facies gradually changed from deep shelf to shallow shelf, which resulted in a large number of graptolites that cannot be deposited and preserved due to the influence of tides and waves in the shallower water, leading to a decrease in graptolite abundance and quantity [21,73–75], as well as a low palaeoproductivity level with low TOC and Si_{bio} content and $Si_{bio}/(Si_{bio} + Fe_{bio} + Al + Ca_{bio})$ ratios (Figures 7 and 10). Overall, these analyses show that palaeoproductivity was high in organic-rich shales with peak values occurring in the lower LLM and significantly low values occurring in organic-lean shales in the Yiling block, and the trend of palaeoproductivity variation is consistent with that found in other regions of the middle-upper Yangtze Platform [12,13,15].

Previous studies have shown that palaeoproductivity is strongly related to the upwelling of nutrients [3] because upwelling can usually bring nutrients from the deep ocean to the shallow shelf, which results in plankton flourishing in surface seawater. The scatter plots show that the $Co \times Mn$ values have a perceptible negative correlation with palaeoproductivity proxies TOC and Si_{bio} in well YD1 (Figure 12a,b), which indicates that palaeoproductivity is apparently influenced by upwelling. Remarkably, palaeoproductivity is primarily controlled by upwelling in the WF and the high TOC and Si_{bio} contents of the four samples with $Co \times Mn$ values of less than 0.4. Additionally, in the region close to the Qinling Ocean (well EHD1) with strong upwelling, palaeoproductivity is higher than that far from the Qinling Ocean (well JY143) (Figure 1c) [12].

5.3. OMA Mechanism

5.3.1. Lithofacies Types Influencing OMA

The sedimentary environment controlled the lithofacies types of shale. Previous studies have suggested that siliceous shale in the Wufeng–Longmaxi Formation has relatively high TOC content, which is beneficial for preserving organic matter [51,53]. The results show that siliceous shale has the highest TOC content (Figure 3d), which is consistent with previous research results [52]. TOC levels are higher in subclass lithofacies S and S-2, and relatively lower in subclass lithofacies M-1 and S-3. Lithofacies S and S-2 are mainly distributed in the WF and LLM with anoxic conditions, high palaeoproductivity, and low terrigenous influx, which are conducive to OMA (Figures 3 and 10). In contrast, lithofacies M-1 is distributed in the WF with low palaeoproductivity and moderate terrigenous influx, and the lithofacies S-3 is mainly distributed in the ULM with oxic conditions, low palaeoproductivity, and high terrigenous influx (Figures 3 and 10). Thus, they are generally not beneficial to OMA.

5.3.2. Main Controlling Factor of OMA

In general, OMA occurred for three reasons: organic matter input (palaeoproductivity), organic matter preservation (palaeoredox conditions and deposition rates), and organic matter dilution (terrigenous detrital influx) [35,76], and the correlations between TOC content and the terrigenous influx proxy Al, deposition rate proxy La_N/Yb_N , palaeoredox proxy Ni/Co, and palaeoproductivity proxy $(Ni + Cu + Zn)_{bio}$ are used to study the main controlling factors of OMA in well YD1. The results show that TOC contents have a weak positive correlation with Al content (Figure 13a), have no obvious correlation with the La_N/Yb_N ratio (Figure 13b), and have an apparent correlation with the Ni/Co ratios and $(Ni + Cu + Zn)_{bio}$ concentrations (Figure 13c,d). These analysis results are consistent with previous studies showing redox conditions and productivity to be the key factors of OMA in the Wufeng–Longmaxi Formation [3,5].

However, we further found that the factors that influence OMA changed vertically (Figure 13e–h). In the WF, TOC contents have a highly positive correlation with Al content, indicating that terrigenous influx is the main controlling factor of OMA, which is significantly different from other regions, inferring that the sedimentation rate of organic matter is higher than the terrigenous dilution rate in well YD1. In the LLM, TOC contents have no correlation with Al content, a weak negative correlation with the La_N/Yb_N ratios, and positive correlations with the Ni/Co ratios and $(Ni + Cu + Zn)_{bio}$ concentrations, indicating that combined redox conditions and productivity influence OMA. In the ULM, TOC contents have strongly negative correlations with Al content and no significant correlations with the La_N/Yb_N and the Ni/Co ratios, as well as the $(Ni + Cu + Zn)_{bio}$ concentrations, indicating that terrigenous influx is the main controlling factor of OMA and implying that terrigenous influx led to the dilution of organic matter, which was not conducive to OMA.

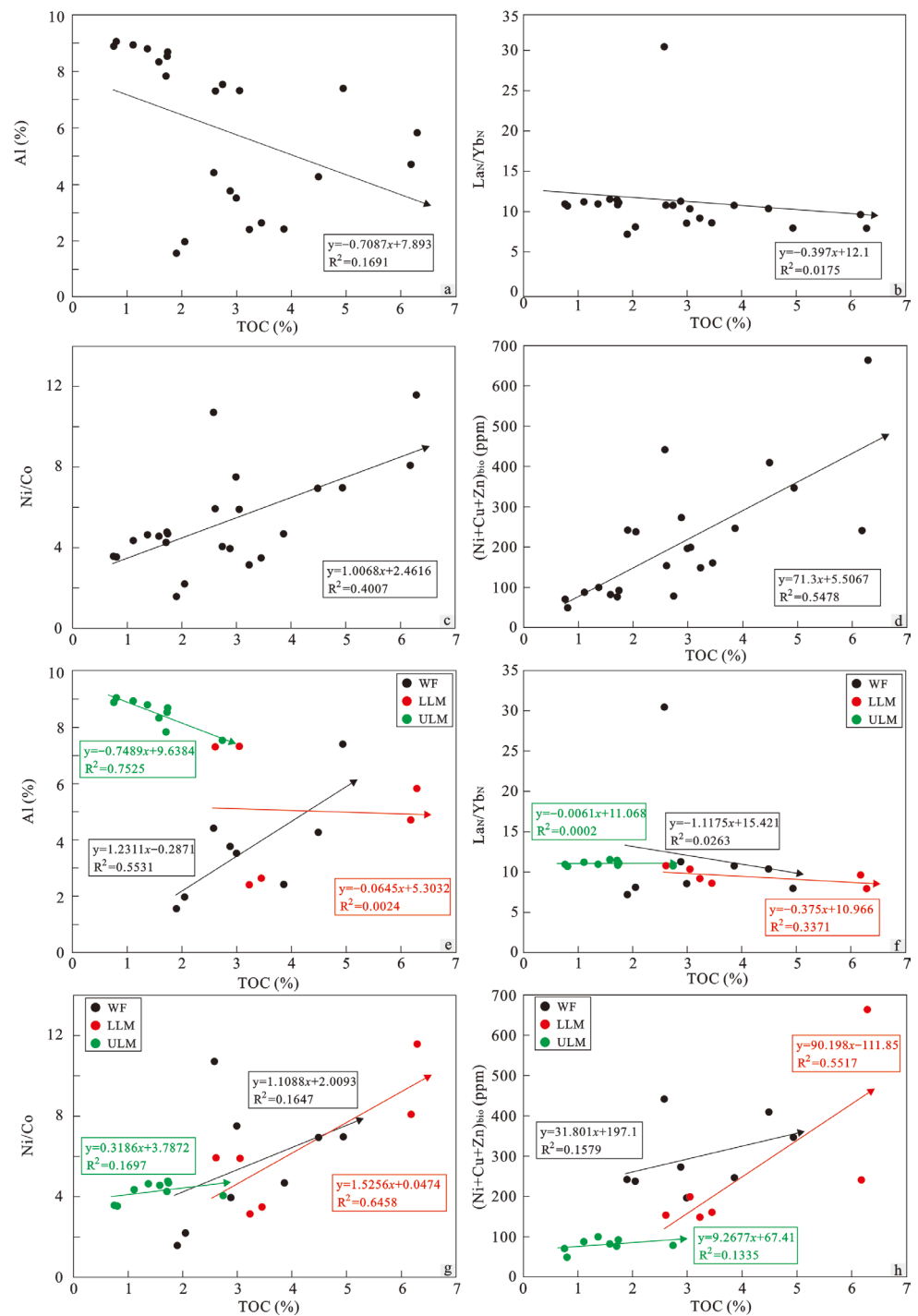


Figure 13. Correlations between TOC content and the factors that influence OMA. (a–d) Crossplots of TOC vs. terrigenous influx proxy Al, deposition rates proxy La_N/Yb_N , palaeoredox proxy Ni/Co, and palaeoproductivity proxy $(Ni + Cu + Zn)_{bio}$ of the Wufeng–Longmaxi Formation, respectively. (e–h) Crossplots of TOC vs. Al, La_N/Yb_N , Ni/Co, and $(Ni + Cu + Zn)_{bio}$ of the WF, LLM, and ULM, respectively. Overall, OMA is controlled by both redox conditions and productivity. However, the factors that influence OMA change vertically, and OMA is mainly influenced by terrigenous influx in the WF and ULM and controlled by redox conditions and productivity in the LLM.

5.4. Evolution Model

A palaeoenvironmental evolutionary model of the Wufeng–Longmaxi Formation is established for the study area, including the LX, WF, GYQ, LLM, and ULM stages

(Figure 14). The routing of the model starts from the Chuanzhong uplift (point A), passes through the Jiaoshiba block, the Hunan–Hubei submarine high, the Yiling block, and ends in the Qinling Ocean (point A') (Figure 1c).

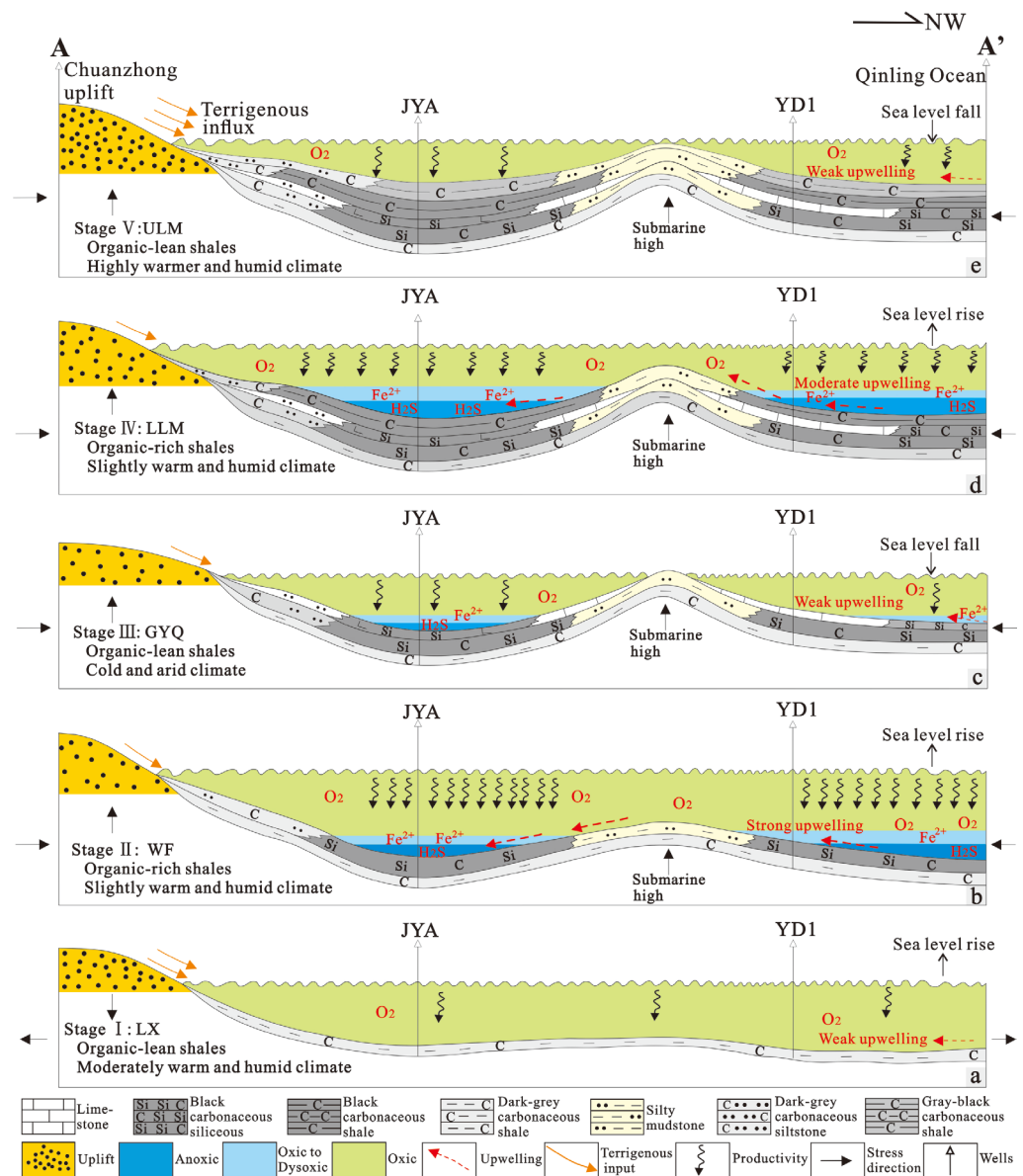


Figure 14. The model of the palaeoenvironmental evolution of the Wufeng–Longmaxi Formation in well YD1. (a) The palaeoenvironmental conditions in the LX stage showing moderate terrigenous influx, moderately warm and humid climate, oxidic conditions and low productivity. (b) The palaeoenvironmental conditions in the WF stage showing low terrigenous influx, slightly warm and humid climate, ferruginous anoxic conditions conditions and high productivity. (c) The palaeoenvironmental conditions in the GYQ stage showing low terrigenous influx, cold and arid climate, oxidic conditions and low productivity. (d) The palaeoenvironmental conditions in the LLM stage showing low terrigenous influx, slightly warm and humid climate, ferruginous to euxinic anoxic conditions conditions and moderate to high productivity. Remarkably, euxinic conditions in the lower LLM are mainly attributed to the rise in sea level caused by the melting of Gondwanan continental glaciers and strong tectonic subsidence caused by continuous compression from the Xuefeng uplift to the Yangtze Platform [16], leading to the formation a deep-water basin. (e) The palaeoenvironmental conditions in the ULM stage showing high terrigenous influx caused by the Kwangsian Orogeny, highly warm and humid climate, oxidic conditions and low productivity.

During the LX stage, the middle-upper Yangtze Platform was deposited under a tension setting [16] with a broad, flat, and shallow sea environment [30]. The palaeoenvironment was characterized by a moderately warm and humid climate, moderate terrigenous influx, low productivity, and oxic bottom water conditions, which were not beneficial to OMA (Figures 7, 10 and 14a).

During the WF stage, the sea level started to rise, and the middle-upper Yangtze platform was deposited under a compressive tectonic setting caused by the subduction of the Cathaysia Block towards the Yangtze Platform [16], which led to the formation of the Hunan-Hubei submarine high and sedimentary depressions. The palaeoenvironment was characterized by a slightly warm and humid climate, low terrigenous influx, anoxic bottom water conditions, and high productivity with strong upwelling, which was conducive to OMA and the formation of black siliceous rock (Figures 7, 10 and 14b).

During the GYQ stage, the Hirnantian glaciation caused a significant drop in global sea levels [16,56], and the Hunan–Hubei submarine high was gradually exposed at Earth’s surface [30]. At this time, the climate was cold and arid [14,77], and weak upwelling led to low productivity in both the middle and upper Yangtze Platforms. The depositional basins were mainly deposited under oxic conditions, except for minor formations in the depocentre of the Sichuan Basin that were still deposited under anoxic conditions [14,78]. The cold glacial climate and poor nutrition in the water body are the important reasons for the global biological extinction event in late Ordovician, with a large number of graptolites disappearing [79]. However, Hirnantia Fauna (Brachiopoda), which benefited from a cold climate and oxygen-rich bottom water, survived (Figures 7, 10 and 14c) [80].

During the LLM, the sea level rose rapidly and seawater formed a stable stratified water body due to the melting of the Gondwanan Glacier [16,64,65]. The palaeoenvironment was characterized by a slightly warm and humid climate, low terrigenous influx, anoxic bottom water and even euxinic conditions (Figure 11), and high palaeoproductivity (Figures 7, 10 and 14d). In addition, the accommodating space of the deep basin significantly increased as a result of continuous tectonic compression [16], leading to the deposition of the thickest organic-rich siliceous and argillaceous shales in the Wufeng–Longmaxi Formation. Remarkably, during the upper LLM stage, the climate became much warmer and wetter, and the sea level gradually dropped due to the strong tectonic uplift as a result of the Kwangsi Orogeny [21,81], which led to dysoxic to oxic bottom water conditions. Meanwhile, the graptolite biozones changed significantly from LM5 in the Rhuddanianto LM6 in the Aeronian (Figures 7 and 10).

During the ULM stage, the palaeoenvironment was characterized by a highly warm and humid climate, similar to that of the upper LLM stage, as well as oxic and low productivity conditions. Remarkably, the Xuefeng uplift continued to rise and was gradually exposed at Earth’s surface, finally forming an uplift due to continuous orogenic movement [16], which became a provenance and supplied terrigenous clasts to the middle-upper Yangtze Platform, leading to the highest terrigenous influx in the Wufeng–Longmaxi Formation, which diluted organic matter and was not conducive to OMA (Figures 7, 10 and 14e).

Overall, organic-rich shales in the WF and LLM of the Yiling block are the high-quality shale gas reservoirs, which are characterized by shale thicknesses of 10–20 m, TOC contents of 3%–4%, and total gas contents of 1–3 m³/t [11]. Although gas contents in the Yiling block are slightly lower than those in the Jiaoshiba block [6,13], prospects for shale gas exploration are still excellent due to high TOC contents, anoxic conditions, and high productivity [2,11]. Remarkably, regions in the eastern Yiling block close to the Qinling Ocean show better prospects for shale gas exploration because of the thicker organic-rich shales caused by deeper water, euxinic bottom water conditions, and higher productivity as a result of the strong upwelling.

6. Conclusions

The Wufeng–Longmaxi shales were primarily deposited in a highly restricted basin, except for the relatively open and upwelling setting of the upper WF. These organic-rich

shales were formed in a warm and humid climate with low terrigenous influx, anoxic conditions, and high productivity. The silica in the shales had a primarily nonhydrothermal origin, with an entirely biogenic source only in the upper WF.

In the southeastern Sichuan Basin, the bottom water of organic-rich shales is mainly characterized by anoxic–euxinic conditions, while in the study area, it is primarily dominated by anoxic–ferruginous conditions, suggesting a shallower water depth.

Compared to previous studies, our research provides further evidence that the Kwangsiang Orogeny had a rapid and significant impact on the palaeoenvironment of the Wufeng–Longmaxi Formation in western Hubei. This environmental shift is observed in the black shale of the LLM stage, resulting in a warmer and wetter climate, a notable decrease in productivity due to inadequate nutrients caused by weak upwelling, an evident increase in terrigenous input, and a shift in bottom water from anoxic to oxic conditions. These changes led to a decrease in graptolite abundance and the transition of graptolite biozones from LM5 to LM6.

Previous studies have established that redox conditions and productivity were the primary controlling factors for OMA, while our research indicates that the factors influencing OMA change vertically, with terrigenous influx mainly influencing OMA in the WF and ULM, and both redox conditions and productivity affecting OMA in the LLM. Notably, the WF stands out from other regions in that TOC contents have a highly positive correlation with Al content, which indicate that the terrigenous influx is the primary factor influencing OMA, suggesting a higher sedimentation rate of organic matter during this stage.

Despite having slightly lower gas contents than the Jiaoshiba block, the organic-rich shales in the WF and LLM of the Yiling block are still considered high-quality shale gas reservoirs with the organic-rich shale thicknesses exceeding 10 meters. Notably, the eastern regions of the Yiling block that are closer to the Qinling Ocean exhibit even better prospects for shale gas exploration.

Author Contributions: Conceptualization, L.X. and Y.W.; methodology, S.H. and M.S.; software, L.X.; validation, L.X., S.H. and Y.W.; formal analysis, L.X.; investigation, L.X.; resources, L.X.; data curation, W.C.; writing—original draft preparation, L.X.; writing—review and editing, S.H. and M.S.; visualization, F.L. and H.Z.; supervision, L.X. and Y.Z.; project administration, Y.Z.; funding acquisition, L.X. All authors have read and agreed to the published version of the manuscript.

Funding: The authors disclosed receipt of the following financial support for the research, authorship, and/or publication of this article: this work is supported by the scientific research project of Department of Natural Resources of Hubei Province (Grant No. ZRZY2021KJ22). The authors also acknowledge fundings by National Natural Science Foundation of China (Nos. 42202155 and 42272159), China Postdoctoral Science Foundation (No. 2021MD703807), Heilongjiang Provincial Postdoctoral Science Foundation (No. LBH-Z20121), China Scholarship Council (No. 202008230018), and Youth Foundation of the Northeast Petroleum University (No. 2019QNL-21).

Institutional Review Board Statement: Not applicable.

Informed Consent Statement: Not applicable.

Data Availability Statement: Data is unavailable due to privacy restrictions.

Acknowledgments: We would like to thank laboratory staff who helped with the experiments. Careful reviews and constructive suggestions of the manuscript by anonymous reviewers are also greatly appreciated.

Conflicts of Interest: The authors declared no potential conflict of interest with respect to the research, authorship, and/or publication of this article.

References

1. Zhang, L.C.; Xiao, D.S.; Lu, S.F.; Jiang, S.; Chen, L.; Guo, T.L.; Wu, L.Y. Pore development of the Lower Longmaxi shale in the southeastern Sichuan Basin and its adjacent areas: Insights from lithofacies identification and organic matter. *Mar. Pet. Geol.* **2020**, *122*, 104662. [[CrossRef](#)]
2. Chen, L.; Jiang, S.; Chen, P.; Chen, X.H.; Zhang, B.M.; Zhang, G.T.; Lin, W.B.; Lu, Y.C. Relative sea-level changes and organic matter enrichment in the Upper Ordovician-Lower Silurian Wufeng-Longmaxi Formations in the Central Yangtze area, China. *Mar. Pet. Geol.* **2021**, *124*, 104809. [[CrossRef](#)]
3. Dong, T.; Wang, C.; Liang, X.; Wang, G.C.; Jiang, S. Paleodepositional conditions and organic matter accumulation mechanisms in the Upper Ordovician-lower Silurian Wufeng-Longmaxi shales, Middle Yangtze region, South China. *Mar. Pet. Geol.* **2022**, *143*, 105823. [[CrossRef](#)]
4. Huang, H.Y.; He, D.F.; Li, Y.Q.; Li, J.; Zhang, L. Silurian tectonic-sedimentary setting and basin evolution in the Sichuan area, southwest China: Implications for palaeogeographic reconstructions. *Mar. Pet. Geol.* **2018**, *92*, 403–423. [[CrossRef](#)]
5. Chen, C.; Mu, C.L.; Zhou, K.K.; Liang, W.; Ge, X.Y.; Wang, X.P.; Wang, Q.Y.; Zheng, B.S. The geochemical characteristics and factors controlling the organic matter accumulation of the Late Ordovician-Early Silurian black shale in the Upper Yangtze Basin, South China. *Mar. Pet. Geol.* **2016**, *76*, 159–175. [[CrossRef](#)]
6. Guo, X.S.; Hu, D.F.; Li, Y.P.; Wei, Z.H.; Wei, X.F.; Liu, Z.J. Geological factors controlling shale gas enrichment and high production in Fuling shale gas field. *Petrol. Explor. Dev.* **2017**, *44*, 513–523. [[CrossRef](#)]
7. Guo, T.L. Key geological issues and main controls on accumulation and enrichment of Chinese shale gas. *Petrol. Explor. Dev.* **2016**, *43*, 349–359. [[CrossRef](#)]
8. Jin, Z.J.; Nie, H.K.; Liu, Q.Y.; Zhao, J.H.; Jiang, T. Source and seal coupling mechanism for shale gas enrichment in upper Ordovician Wufeng Formation—Lower Silurian Longmaxi Formation in Sichuan Basin and its periphery. *Mar. Pet. Geol.* **2018**, *97*, 78–93. [[CrossRef](#)]
9. Tang, X.L.; Jiang, S.; Jiang, Z.X.; Li, Z.; He, Z.L.; Long, S.X.; Zhu, D.Y. Heterogeneity of Paleozoic Wufeng-Longmaxi formation shale and its effects on the shale gas accumulation in the Upper Yangtze Region, China. *Fuel* **2019**, *239*, 387–402. [[CrossRef](#)]
10. Yi, J.Z.; Bao, H.Y.; Zheng, A.W.; Zhang, B.Q.; Shu, Z.G.; Li, J.Q.; Wang, C. Main factors controlling marine shale gas enrichment and high-yield wells in South China: A case study of the Fuling shale gas field. *Mar. Pet. Geol.* **2019**, *103*, 114–125. [[CrossRef](#)]
11. Cai, Q.S.; Chen, X.H.; Zhang, B.M.; Liu, A.; Han, J.; Zhang, G.T.; Li, Y.G. Origin of siliceous minerals in the black shale of the Wufeng and Longmaxi Formations in the Yichang area, western Hubei Province: Geological significance for shale gas. *Acta Geol. Sin.* **2020**, *94*, 931–946.
12. Lu, Y.B.; Jiang, S.; Lu, Y.C.; Xu, S.; Shu, Y.; Wang, Y.X. Productivity or preservation? The factors controlling the organic matter accumulation in the late Katian through Hirnantian Wufeng organic-rich shale, South China. *Mar. Pet. Geol.* **2019**, *109*, 22–35. [[CrossRef](#)]
13. Wang, Y.X.; Xu, S.; Hao, F.; Lu, Y.B.; Shu, Z.G.; Yan, D.T.; Lu, Y.C. Geochemical and petrographic characteristics of Wufeng-Longmaxi shales, Jiaoshiba area, southwest China: Implications for organic matter differential accumulation. *Mar. Pet. Geol.* **2019**, *102*, 138–154. [[CrossRef](#)]
14. Yan, D.T.; Chen, D.Z.; Wang, Z.Z.; Li, J.; Yang, X.R.; Zhang, B. Climatic and oceanic controlled deposition of Late Ordovician-Early Silurian black shales on the North Yangtze platform, South China. *Mar. Pet. Geol.* **2019**, *110*, 112–121.
15. Zhang, L.C.; Xiao, D.S.; Lu, S.; Jiang, S.; Lu, S.F.; Jiang, S.; Lu, S.D. Effect of sedimentary environment on the formation of organic-rich marine shale: Insights from major/trace elements and shale composition. *Int. J. Coal Geol.* **2019**, *204*, 34–50. [[CrossRef](#)]
16. Huang, H.Y.; He, D.F.; Li, D.; Li, Y.Q.; Zhang, W.K.; Chen, J.J. Geochemical characteristics of organic-rich shale, Upper Yangtze Basin: Implications for the Late Ordovician–Early Silurian orogeny in South China. *Paleogeogr. Paleoclimatol. Paleoecol.* **2020**, *554*, 109822. [[CrossRef](#)]
17. Lei, Z.H.; Dashtgard, S.E.; Wang, J.; Li, M.; Feng, Q.L.; Yu, Q.; Zhao, A.K.; Du, L.T. Origin of chert in Lower Silurian Longmaxi Formation: Implications for tectonic evolution of Yangtze Block, South China. *Paleogeogr. Paleoclimatol. Paleoecol.* **2019**, *529*, 53–66. [[CrossRef](#)]
18. Brenchley, P.J.; Marshall, J.D.; Carden, G.A.F.; Robertson, D.B.R.; Long, D.G.F.; Meidla, T.; Anderson, T.F. Bathymetric and isotopic evidence for a short-lived Late Ordovician glaciation in a greenhouse period. *Geology* **1994**, *22*, 295–298. [[CrossRef](#)]
19. Yao, W.H.; Li, Z.X. Tectonostratigraphic history of the Ediacaran-Silurian Nanhua foreland basin in South China. *Tectonophysics* **2016**, *674*, 31–51. [[CrossRef](#)]
20. Chen, X.; Zhang, Y.D.; Fan, J.X.; Tang, L.; Sun, H.Q. Onset of the Kwangsian Orogeny as evidenced by biofacies and lithofacies. *Sci. China Earth Sci.* **2012**, *55*, 1592–1600. [[CrossRef](#)]
21. Chen, X.; Chen, Q.; Zhen, Y.Y.; Wang, H.Y.; Zhang, L.N.; Zhang, J.P.; Wang, W.H.; Xiao, Z.H. Circumjacent distribution pattern of the Lungmachiian graptolitic black shale (early Silurian) on the Yichang Uplift and its peripheral region. *Sci. China Earth Sci.* **2018**, *61*, 1195–1203. [[CrossRef](#)]
22. Li, N.; Algeo, T.J.; Cheng, M.; Jin, C.S.; Zhu, G.Y.; Fan, J.X.; Sun, Z.Y. Redox changes in the outer Yangtze Sea (South China) through the Hirnantian Glaciation and their implications for the end-Ordovician biocrisis. *Earth-Sci. Rev.* **2021**, *212*, 103443. [[CrossRef](#)]

23. Li, N.; Li, C.; Fan, J.X.; Algeo, T.J.; Yan, D.T.; Zhu, G.Y.; Wu, S.Y.; Tang, S.D.; Cheng, M.; Jin, C.S. Sulfate-controlled marine euxinia in the semi-restricted inner Yangtze Sea (South China) during the Ordovician-Silurian transition. *Paleogeogr. Paleoclimatol. Paleocol.* **2019**, *534*, 109–281. [[CrossRef](#)]
24. Jin, C.S.; Liao, Z.W.; Lash, G.G. High-frequency redox variation across the Ordovician–Silurian transition, South China. *Paleogeogr. Paleoclimatol. Paleocol.* **2021**, *566*, 110218. [[CrossRef](#)]
25. Zhou, X.L.; Liu, Y.; Cao, H.Y.; Zhong, H.T.; Li, Y.C. Responses of oceanic chemistry to climatic perturbations during the Ordovician-Silurian transition: Implications for geochemical proxies and organic accumulations. *Mar. Pet. Geol.* **2021**, *134*, 105341. [[CrossRef](#)]
26. Tribovillard, N.; Bialkowski, A.; Tyson, R.V.; Lallier-Verges, E.; Deconinck, J.F. Organic facies variations in the late Kimmeridgian of the Boulonnais area (northernmost France). *Mar. Petrol. Geol.* **2001**, *18*, 371–389. [[CrossRef](#)]
27. Rimmer, S.M.; Thompson, J.A.; Goodnight, S.A.; Robl, T.L. Multiple controls on the preservation of organic matter in Devonian–Mississippian marine black shales: Geochemical and petrographic evidence. *Paleogeogr. Paleoclimatol. Paleocol.* **2004**, *215*, 125–154. [[CrossRef](#)]
28. Sageman, B.B.; Murphy, A.E.; Werne, J.P.; Straeten, C.A.V.; Hollander, D.J.; Lyons, T.W. A tale of shales: The relative roles of production, decomposition, and dilution in the accumulation of organic-rich strata, Middle-Upper Devonian, Appalachian basin. *Chem. Geol.* **2003**, *195*, 229–273. [[CrossRef](#)]
29. Wang, X.; Tian, J.C.; Lin, X.B.; Chen, W.Z.; Yi, D.X. Sedimentary Environment and Controlling Factors of Organic Matter Accumulation in Wufeng-Longmaxi Formations: A case study of Jielong section in eastern Chongqing. *Acta Sedimentol. Sin.* **2022**. [[CrossRef](#)]
30. Rong, J.Y.; Chen, X. Faunal differentiation, biofacies and lithofacies pattern of late Ordovician (Ashgillian) in south China. *Acta Palaeontol. Sin.* **1987**, *26*, 507–535.
31. Poulton, S.W.; Canfield, D.E. Development of a sequential extraction procedure for iron: Implications for iron partitioning in continentally derived particulates. *Chem. Geol.* **2005**, *214*, 209–221. [[CrossRef](#)]
32. Tribovillard, N.; Algeo, T.J.; Lyons, T.; Riboulleau, A. Trace metals as paleoredox and paleoproductivity proxies: An update. *Chem. Geol.* **2006**, *232*, 12–32. [[CrossRef](#)]
33. Ross, D.J.K.; Bustin, R.M. Investigating the use of sedimentary geochemical proxies for paleoenvironment interpretation of thermally mature organic-rich strata: Examples from the Devonian-Mississippian shales, Western Canadian Sedimentary Basin. *Chem. Geol.* **2009**, *260*, 1–19. [[CrossRef](#)]
34. Wang, X.Q.; Zhu, Y.M.; Lash, G.G.; Wang, Y. Multi-proxy analysis of organic matter accumulation in the Upper Ordovician–Lower Silurian black shale in the upper Yangtze Platform, south China. *Mar. Pet. Geol.* **2019**, *103*, 473–484. [[CrossRef](#)]
35. Wu, W.; Liu, W.Q.; Mou, C.L.; Liu, H.; Qiao, Y.; Pan, J.N.; Ning, S.Y.; Zhang, X.X.; Yao, J.X.; Liu, J.D. Organic-rich siliceous rocks in the upper Permian Dalong Formation (NW middle Yangtze): Provenance, paleoclimate and paleoenvironment. *Mar. Pet. Geol.* **2021**, *123*, 104728. [[CrossRef](#)]
36. Nesbitt, H.W.; Young, G.M. Early proterozoic climates and plate motions inferred from major element chemistry of lutites. *Nature* **1982**, *299*, 715–717. [[CrossRef](#)]
37. Bhatia, M.R.; Crook, K.A.W. Trace element characteristics of graywackes and tectonic setting discrimination of sedimentary basins. *Contrib. Mineral. Petrol.* **1986**, *92*, 181–193. [[CrossRef](#)]
38. Ge, X.Y.; Mou, C.L.; Yu, Q.; Liu, W.; Men, X.; He, J.L. The geochemistry of the sedimentary rocks from the Huadi No. 1 well in the Wufeng-Longmaxi formations (Upper Ordovician-Lower Silurian), South China, with implications for paleoweathering, provenance, tectonic setting and paleoclimate. *Mar. Pet. Geol.* **2019**, *103*, 646–660. [[CrossRef](#)]
39. Fritz, M.; Unkel, I.; Lenz, J.; Gajewski, K.; Frenzel, P.; Paquette, N.; Lantuit, H.; Körte, L.; Wetterich, S. Regional environmental change versus local signal preservation in Holocene thermokarst lake sediments: A case study from Herschel Island, Yukon (Canada). *J. Paleolimnol.* **2018**, *60*, 77–96. [[CrossRef](#)]
40. Xu, C.; Shan, X.L.; He, W.T.; Zhang, K.; Rexiti, Y.L.K.; Su, S.Y.; Liang, C.; Zou, X.T. The influence of paleoclimate and a marine transgression event on organic matter accumulation in lacustrine black shales from the Late Cretaceous, southern Songliao Basin, Northeast China. *Int. J. Coal Geol.* **2021**, *246*, 103842. [[CrossRef](#)]
41. Shi, J.; Zou, Y.R.; Cai, Y.L.; Zhan, Z.W.; Sun, J.N.; Liang, T.; Peng, P.A. Organic matter enrichment of the Chang 7 member in the Ordos Basin: Insights from chemometrics and element geochemistry. *Mar. Pet. Geol.* **2022**, *135*, 105404. [[CrossRef](#)]
42. Rimmer, S.M. Geochemical paleoredox indicators in Devonian Mississippian black shales, central Appalachian basin (USA). *Chem. Geol.* **2004**, *206*, 373–391. [[CrossRef](#)]
43. Lyons, T.W.; Severmann, S. A critical look at iron paleoredox proxies: New insights from modern euxinic marine basins. *Geochim. Cosmochim. Acta* **2006**, *70*, 5698–5722. [[CrossRef](#)]
44. Trela, W.; Podhalańska, T.; Smolarek, J.; Marynowski, L. Llandovery green/grey and black mudrock facies of the northern Holy Cross Mountains (Poland) and their relation to early Silurian sea-level changes and benthic oxygen level. *Sediment. Geol.* **2016**, *342*, 66–77. [[CrossRef](#)]
45. Smolarek, J.; Marynowski, L.; Trela, W.; Kujawski, P.; Simoneit, B.R.T. Redox conditions and marine microbial community changes during the end-Ordovician mass extinction event. *Global Planet Change* **2017**, *149*, 105–122. [[CrossRef](#)]

46. Yuan, Y.Y.; Cai, C.F.; Wang, T.K.; Xiang, L.; Jia, L.Q.; Chen, Y. Redox condition during Ediacaran-Cambrian transition in the Lower Yangtze deep water basin, South China: Constraints from iron speciation and $\delta^{13}\text{C}_{\text{org}}$ in the Diben section, Zhejiang. *Chin. Sci. Bull.* **2014**, *59*, 3638–3649. [[CrossRef](#)]
47. Lei, L.D.; Shen, J.; Li, C.; Algeo, T.J.; Chen, Z.Q.; Feng, Q.L.; Cheng, M.; Jin, C.S.; Huang, J.H. Controls on regional marine redox evolution during Permian-Triassic transition in South China. *Paleogeogr. Paleoclimatol. Paleocol.* **2017**, *486*, 17–32. [[CrossRef](#)]
48. Ma, Y.Q.; Fan, M.J.; Lu, Y.C.; Guo, X.S.; Hu, H.Y.; Chen, L.; Wang, C.; Liu, X.C. Geochemistry and sedimentology of the Lower Silurian Longmaxi mudstone in southwestern China: Implications for depositional controls on organic matter accumulation. *Mar. Petrol. Geol.* **2016**, *75*, 291–309. [[CrossRef](#)]
49. Sweere, T.; van den Boorn, S.; Dickson, A.J.; Reichart, G.J. Definition of new trace-metal proxies for the controls on organic matter enrichment in marine sediments based on Mn, Co, Mo and Cd concentrations. *Chem. Geol.* **2016**, *441*, 235–245. [[CrossRef](#)]
50. Nancet, W.B.; Taylor, S.R. Rare earth element patterns and crustal evolution—I. Australian post-Archean sedimentary rocks. *Geochim. Cosmochim. Acta* **1976**, *40*, 1539–1551. [[CrossRef](#)]
51. Wang, C.; Zhang, B.Q.; Shu, Z.G.; Lu, Y.C.; Lu, Y.Q.; Bao, H.Y.; Li, Z.; Liu, C. Lithofacies types and reservoir characteristics of marine shales of the Wufeng Formation-Longmaxi Formation in Fuling area, the Sichuan Basin. *Oil Gas Geol.* **2018**, *39*, 485–497.
52. Wang, E.Z.; Guo, T.L.; Li, M.W.; Li, C.R.; Dong, X.X.; Zhang, N.X.; Feng, Y. Exploration potential of different lithofacies of deep marine shale gas systems: Insight into organic matter accumulation and pore formation mechanisms. *Mar. Petrol. Geol.* **2022**, *102*, 104563. [[CrossRef](#)]
53. Zhai, G.Y.; Wang, Y.F.; Liu, G.H.; Lu, Y.C.; He, S.; Zhou, Z.; Li, J.; Zhang, Y. Accumulation model of the Sinian-Cambrian shale gas in western Hubei Province, China. *J. Geomech.* **2020**, *26*, 696–713.
54. Adegoke, A.K.; Abdullah, W.H.; Hakimi, M.H.; Sarki Yandoka, B.M. Geochemical characterisation of Fika Formation in the Chad (Bornu) Basin, northeastern Nigeria: Implications for depositional environment and tectonic setting. *Appl. Geochem.* **2014**, *43*, 1–12. [[CrossRef](#)]
55. Chang, H.; An, Z.S.; Wu, F.; Jin, Z.D.; Liu, W.G.; Song, Y.G. A Rb/Sr record of the weathering response to environmental changes in westerly winds across the Tarim Basin in the late Miocene to the early Pleistocene. *Paleogeogr. Paleoclimatol. Paleocol.* **2013**, *386*, 364–373. [[CrossRef](#)]
56. Haq, B.U.; Schutter, S.R. A chronology of Paleozoic sea-level changes. *Science* **2008**, *322*, 64–68. [[CrossRef](#)] [[PubMed](#)]
57. Van den Boorn, S.H.J.M.; van Bergen, M.J.; Nijman, W.; Vroon, P.Z. Dual role of seawater and hydrothermal fluids in Early Archean chert formation: Evidence from silicon isotopes. *Geology* **2007**, *35*, 939–942. [[CrossRef](#)]
58. Khan, M.Z.; Feng, Q.L.; Zhang, K.; Guo, W. Biogenic silica and organic carbon fluxes provide evidence of enhanced marine productivity in the Upper Ordovician-Lower Silurian of South China. *Paleogeogr. Paleoclimatol. Paleocol.* **2019**, *534*, 109–278. [[CrossRef](#)]
59. Garbán, G.; Martínez, M.; Márquez, G.; Rey, O.; Escobar, M.; Esquinas, N. Geochemical signatures of bedded cherts of the upper La Luna Formation in Táchira State, western Venezuela: Assessing material provenance and paleodepositional setting. *Sediment. Geol.* **2017**, *347*, 130–147. [[CrossRef](#)]
60. Chen, X.; Fan, J.X.; Chen, Q.; Tang, L.; Hou, X.D. Toward a stepwise Kwangian Orogeny. *Sci. China Earth Sci.* **2014**, *57*, 379–387. [[CrossRef](#)]
61. Jones, B.; Manning, D.A.C. Comparison of geochemical indices used for the interpretation of palaeoredox conditions in ancient mudstones. *Chem. Geol.* **1994**, *111*, 111–129. [[CrossRef](#)]
62. Algeo, T.J.; Maynard, J.B. Trace-element behavior and redox facies in core shales of Upper Pennsylvanian Kansas-type cyclothems. *Chem. Geol.* **2004**, *206*, 289–318. [[CrossRef](#)]
63. Poulton, S.W.; Canfield, D.E. Ferruginous conditions: A dominant feature of the ocean through Earth’s history. *Elements* **2011**, *7*, 107–112. [[CrossRef](#)]
64. Kwak, D.H.; Song, Y.S.; Choi, Y.H.; Kim, K.M.; Jeong, Y.H. Influence of sluice gate operation on salinity stratification and hypoxia development in a brackish estuary dam. *Reg. Stud. Mar. Sci.* **2023**, *57*, 102731. [[CrossRef](#)]
65. Van Soelen, E.E.; Twitchett, R.J.; Kürschner, W.M. Salinity changes and anoxia resulting from enhanced run-off during the late Permian global warming and mass extinction event. *Clim. Past* **2018**, *14*, 441–453. [[CrossRef](#)]
66. Algeo, T.J.; Tribovillard, N. Environmental analysis of paleoceanographic systems based on molybdenum–uranium covariation. *Chem. Geol.* **2009**, *268*, 211–225. [[CrossRef](#)]
67. Algeo, T.J.; Lyons, T.W. Mo-total organic carbon covariation in modern anoxic marine environments: Implications for analysis of paleoredox and paleohydrographic conditions. *Paleoceanography* **2006**, *21*, PA101623. [[CrossRef](#)]
68. Zhang, J.F.; Xu, H.; Zhou, Z.; Ren, P.F.; Guo, J.Z.; Wang, Q. Geological characteristics of shale gas reservoir in Yichang area, western Hubei. *Acta Pet. Sin.* **2019**, *40*, 887–899.
69. Canfield, D.E. Factors influencing organic carbon preservation in marine sediments. *Chem. Geol.* **1994**, *114*, 315–329. [[CrossRef](#)]
70. Zhang, K.; Li, X.; Wang, Y.; Liu, W.; Yu, Y.; Zhou, L.; Feng, W. Paleo-environments and organic matter enrichment in the shales of the Cambrian Niutitang and Wunitang Formations, south China: Constraints from depositional environments and geochemistry. *Mar. Pet. Geol.* **2021**, *134*, 105329. [[CrossRef](#)]
71. Brumsack, H.J. The trace metal content of recent organic carbon-rich sediments: Implications for cretaceous black shale formation. *Palaeogeogr. Palaeoclimatol. Palaeocol.* **2006**, *232*, 344–361. [[CrossRef](#)]

72. Algeo, T.J.; Kuwahara, K.; Sano, H.; Bates, S.; Lyons, T.; Elswick, E.; Maynard, J.B. Spatial variation in sediment fluxes, redox conditions, and productivity in the Permian–Triassic Panthalassic Ocean. *Palaeogeogr. Palaeoclimatol. Palaeoecol.* **2011**, *308*, 65–83. [[CrossRef](#)]
73. Cai, Q.S.; Chen, X.H.; Wang, C.S.; Zhang, B.M.; Han, J.; Zhang, G.T.; Liu, A.; Luo, S.Y.; Li, H.; Zhang, M.; et al. Occurrence characteristics and depositional model of Graptolites from the black shale in the Upper Ordovician Wufeng Formation and lower Silurian Longmaxi Formation. *Bull. Geol. Sci. Tech.* **2020**, *39*, 43–53.
74. Wang, H.Y.; Shi, Z.S.; Sun, S.S. Biostratigraphy and reservoir characteristics of the Ordovician Wufeng Formation Silurian Longmaxi Formation shale in the Sichuan Basin and its surrounding areas, China. *Petrol. Explor. Dev.* **2021**, *48*, 1019–1032. [[CrossRef](#)]
75. Qiu, Z.; Zou, C.N.; Li, X.Z.; Wang, H.Y.; Dong, D.Z.; Lu, B.; Zhou, S.W.; Shi, Z.S.; Feng, Z.Q.; Zhang, M.Q. Discussion on the contribution of graptolite to organic enrichment and gas shale reservoir: A case study of the Wufeng–Longmaxi shales in South China. *J. Nat. Gas Geosci.* **2018**, *3*, 147–156. [[CrossRef](#)]
76. Cirilli, S.; Panfili, G.; Buratti, N.; Frixia, A. Paleoenvironmental reconstruction by means of palynofacies and lithofacies analyses: An example from the Upper Triassic subsurface succession of the Hyblean Plateau Petroleum System (SE Sicily, Italy). *Rev. Paleobot. Palynol.* **2018**, *253*, 70–87. [[CrossRef](#)]
77. Armstrong, H.A.; Turner, B.R.; Makhlof, I.M.; Weedon, G.P.; Williams, M.; Al Smadi, A.; Salah, A.A. Origin, sequence stratigraphy and depositional environment of an upper Ordovician (Hirnantian) deglacial black shale, Jordan. *Palaeogeogr. Palaeoclimatol. Palaeoecol.* **2005**, *220*, 273–289. [[CrossRef](#)]
78. Wang, Y.M.; Dong, D.Z.; Huang, J.L.; Li, X.J.; Wang, S.F. Guanyinqiao Member lithofacies of the Upper Ordovician Wufeng Formation around the Sichuan Basin and the significance to shale gas plays, SW China. *Petrol. Explor. Dev.* **2016**, *43*, 42–50. [[CrossRef](#)]
79. Finnegan, S.; Heim, N.A.; Peters, S.E.; Fischer, W.W. Climate change and the selective signature of the Late Ordovician mass extinction. *Proc. Natl. Acad. Sci. USA* **2012**, *109*, 6829–6834. [[CrossRef](#)]
80. Rong, J.Y.; Chen, X.; Happer, D.A.T. The latest Ordovician Hirnantia Fauna (Brachiopoda) in time and space. *Lethaia* **2002**, *35*, 231–249.
81. Yang, X.R.; Yan, D.T.; Zhang, B.; Zhang, L.W.; Wei, X.S.; Li, T.; He, J.; Shangguan, Y.F.; Zhang, M.X.; She, X.H. The depositional mechanism of organic-rich siliceous shales in Upper Yangtze area: Response to the Kwangian Orogeny in South China. *J. Pet. Sci. Eng.* **2020**, *192*, 107–310. [[CrossRef](#)]

Disclaimer/Publisher’s Note: The statements, opinions and data contained in all publications are solely those of the individual author(s) and contributor(s) and not of MDPI and/or the editor(s). MDPI and/or the editor(s) disclaim responsibility for any injury to people or property resulting from any ideas, methods, instructions or products referred to in the content.